Bio-Design and Manufacturing (2025) 8:288–309
https://doi.org/10.1631/bdm.2400248

RESEARCH ARTICLE

Hydroxy-α-sanshool-loaded adipose-targeted mesoporous silica nanoparticles induce white adipose browning and reduce obesity by activating TRPV1

Qing Zhang[1,2] · Chengxun He[1] · Juan Guo[1] · Dandan Tang[1] · Die Qian[1] · Chuan Zheng[3,4] · Chunjie Wu[1] · Wei Peng[1]

Received: 24 June 2024 / Accepted: 21 September 2024 / Published online: 1 March 2025

Abstract

Obesity has become a global threat to health; however, the available drugs for treating obesity are limited. We investigated the anti-obesity effect of hydroxy-α-sanshool (HAS), an amide derived from the fruit of *Zanthoxylum bungeanum*, which promotes the management of obesity by triggering the browning of white adipose tissue (WAT) targeting the membrane receptor of transient receptor potential vanilloid 1 (TRPV1). However, HAS easily undergoes configuration transformation and oxidative degradation. The short peptide CKGGRAKDC or adipose-targeting sequence (ATS) binds specifically to prohibitin on the surface of WAT cells and can be used as recognition assembly to enhance adipocyte targetability. Furthermore, mesoporous silica nanoparticles (MSNs) are widely used in drug delivery systems because of their large specific surface area and pore volume. Therefore, HAS-loaded adipose-targeted MSNs (MSNs-ATS) were developed to enhance the adipocyte targetability, safety, and efficacy of HAS, and tested on mature 3T3-L1 cells and obese mouse models. MSNs-ATS showed higher specificity for adipocyte targetability without obvious toxicity. HAS-loaded MSNs-ATS showed anti-obesity effects superior to those of HAS alone. In conclusion, we successfully developed adipocyte-targeted, HAS-loaded MSNs with good safety and anti-obesity effects.

Graphical abstract

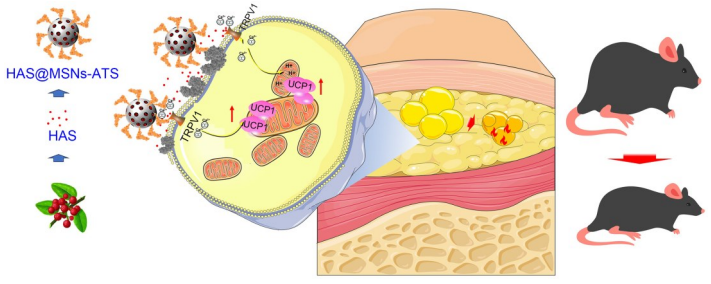

Keywords Hydroxy-α-sanshool · Adipocyte targetability · Mesoporous silica nanoparticles · White adipose tissue browning · Obesity

✉ Chuan Zheng
zhengchuan@cdutcm.edu.cn

✉ Chunjie Wu
wuchunjie@cdutcm.edu.cn

✉ Wei Peng
pengwei@cdutcm.edu.cn

[1] State Key Laboratory of Southwestern Chinese Medicine Resources, School of Pharmacy, Innovative Institute of Chinese Medicine and Pharmacy/Academy for Interdiscipline, Chengdu University of Traditional Chinese Medicine, Chengdu 611130, China

[2] Department of Molecular & Integrative Physiology, University of Michigan, Ann Arbor, Michigan 48109, USA

[3] TCM Regulating Metabolic Diseases Key Laboratory of Sichuan Province, Hospital of Chengdu University of Traditional Chinese Medicine, Chengdu 610072, China

[4] Sichuan Provincial Engineering Research Center of Innovative Re-development of Famous Classical Formulas, Tianfu TCM Innovation Harbour, Chengdu University of Traditional Chinese Medicine, Chengdu 611930, China

1 Introduction

Owing to ever-improving living standards and ever-changing dietary habits, the prevalence of obesity is increasing sharply all over the world and has become a serious global health threat [1–3]. Previous studies have found that the main cause of obesity is a higher energy intake than expenditure, which results in the storage of excess energy as fat in the abdomen, back, legs, and liver [4]. Accumulating evidence demonstrates that obesity is closely related to the development of many diseases, such as diabetes, cardiovascular disease, fatty liver, and even cancer [5, 6]. Obesity has become a serious challenge to human health with limited therapeutic options currently available, mainly diet management, exercise, surgery, and drug therapy [7]. Diet management and exercise are considered to be the healthiest ways to reverse obesity; however, they have a low success rate and a risk of relapse. While most of the slimming drugs available can control energy intake by suppressing appetite (e.g., phentermine) or reducing nutrient absorption (e.g., orlistat), these drugs cause adverse events, such as insomnia, urticaria, and pulmonary hypertension or unpalatable side effects (such as oily stool and fecal incontinence), as well as a risk of relapse [8–12]. Furthermore, while surgical treatment is effective, it is costly, and invasive surgery can cause injury. Studies have increasingly reported a more efficient and healthy way of treating obesity by promoting the browning of white adipose tissue (WAT) [13–16]. Brown adipose tissue (BAT) has higher metabolic efficiency and energy consumption [17–19]; can fully burn free fatty acids, glucose, and other metabolites; and consume excess energy in the body through heat production mediated by uncoupling protein 1 (UCP-1), which is expressed in the inner mitochondrial membrane [20–22].

Hydroxy-α-sanshool (HAS) is an unsaturated chain fatty acid amide alkaloid derived from the fruit of *Zanthoxylum bungeanum* Maxim. Consistent with previous reports [23, 24], we found that HAS exhibits strong anti-obesity effects. One of the important underlying molecular mechanisms involves the activation of the cell membrane receptor of transient receptor potential vanilloid 1 (TRPV1) cation channel and the promotion of WAT browning [25, 26]. Although HAS showed good anti-obesity effects both in vivo and in vitro, the special structure of HAS makes it insoluble in water and prone to configuration transformation and oxidative degradation, which seriously limits its drug development [27, 28]. Temperature, oxygen, ultraviolet (UV) radiation, pH, and artificial stomach/intestinal fluid affect the stability of HAS [28]. We previously found that the degradation rates of HAS were 82.2% and 58.0% after 8 h exposure to artificial gastric juice and ultraviolet light, respectively [29]. Therefore, modern drug delivery systems must be developed to improve the solubility, stability, and patient compliance of HAS.

Mesoporous silica nanoparticles (MSNs) are widely used in drug delivery systems because of their simple synthesis, good biocompatibility, regular pore structure, and large specific surface area and pore volume [30–33]. The loading of HAS into MSNs would not only improve the water solubility and stability of the drug, but also reduce irritation induced by HAS. Prohibitin is pivotal in the regulation of the cell cycle and mitochondrial function and is highly expressed on the cell membrane of mature adipocytes. In 2004, Kolonin et al. reported that the short peptide CKGGRAKDC or adipose-targeting sequence (ATS) can specifically bind to prohibitin on the surface of WAT cells, which can be incorporated into an efficient adipocyte-targeted delivery system [34, 35]. In the present study, we developed an HAS-loaded MSN drug delivery system modified with ATS to enhance adipose tissue targetability. Furthermore, differentiated mature adipocyte and obese mouse models were established to systematically study the anti-obesity activity of HAS-loaded ATS-modified MSNs in vitro (Fig. 1).

2 Materials and methods

2.1 Chemicals and reagents

Tetraethyl orthosilicate (TEOS), cetyltrimethylammonium bromide (CTAB), 3-aminopropyltriethoxysilane (APTES), N-hydroxy-succinimide (NHS), 1-(3-dimethylaminopropyl)-3-ethylcarbodiimide hydrochloride (EDC), and other analytically pure inorganic reagents were obtained from the Chengdu Chronchem Reagent Company (Chengdu, China). HAS was purchased from Chengdu Materia Medica Tianyun Biotech Co., Ltd. (Chengdu, China). LysoTracker probe, 1,1-dioctadecyl-3,3,3,3-tetramethylindotricarbocyaine iodide (DIR), fluorescein isothiocyanate (FITC), rhod-2 acetoxymethyl ester (rhod-2 AM) probe, and MitoTracker probe were purchased from Yeasen Bio Ltd. (Shanghai, China). Dimethyl sulfoxide (DMSO), cell counting kit (CCK)-8 detection kit, bicinchoninic acid (BCA) protein concentration kit, horseradish peroxidase (HRP)-conjugated AffiniPure goat anti-rabbit/mouse IgG (H+L), and anti-β-actin were obtained from Wuhan Bode Biological Co., Ltd. (Wuhan, China). ATS was acquired from GL Biochem (Shanghai) Ltd. (Shanghai, China). Alanine aminotransferase (ALT), aspartate aminotransferase (AST), total cholesterol (TC), triglycerides (TG), and other biochemical detection kits were acquired from Nanjing Jiancheng Biological Co., Ltd. (Nanjing, China). Pentobarbital sodium was acquired from Sigma-Aldrich (Shanghai, China). Primary antibodies for UCP1 and TRPV1 were purchased from ABclonal Biol. Ltd. (Shanghai, China). Enhanced chemiluminescence (ECL) reagents were obtained from Beijing Sizhengbai Biological Co., Ltd. (Beijing, China). Tri-color pre-stained protein standards were obtained from Hunan Aikerui Co., Ltd. (Shenzhen, China).

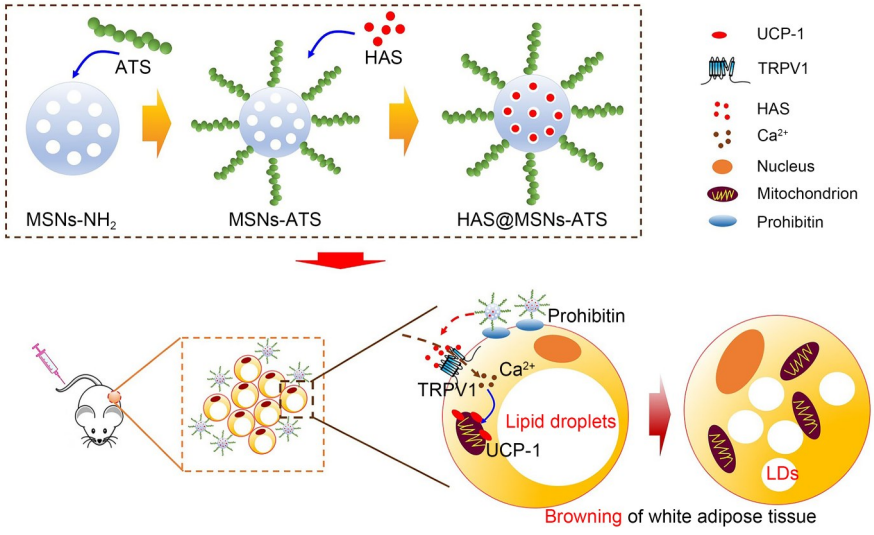

Fig. 1 Design of HAS-loaded nanoparticles for obesity therapy. The MSN surface was modified by the short peptide ATS CKGGRAKDC to enhance its adipocyte targetability. The prepared adipose-targeted MSNs (MSNs-ATS) were loaded into the HAS (HAS@MSNs-ATS). Compared with HAS alone, HAS@MSNs-ATS exhibited better adipocyte targetability and anti-obesity effects in obese mice by promoting white adipose tissue browning by activating TRPV1. HAS: hydroxy-α-sanshool; MSN: mesoporous silica nanoparticle; ATS: adipose-targeting sequence; TRPV1: transient receptor potential vanilloid 1; LD: lipid droplet; UCP-1: uncoupling protein 1

2.2 Preparation and characteristics of nanoparticles

MSNs were prepared according to the classical Stober's method but with optimization of the synthesis method [36–40]. Briefly, 90% ethanol (EtOH), CTAB (0.10 g), 2 mol/L sodium hydroxide (NaOH) solution (0.35 mL), and ultra-pure water were mixed in a three-necked flask and placed in an oil bath at 85 °C under rapid stirring. Subsequently, 0.60 mL TEOS was dissolved into 2 mL anhydrous EtOH and quickly added to the three-necked flask for further reaction for 3 h. Afterward, the reaction products were collected and washed repeatedly with anhydrous EtOH and deionized water solution and were subsequently condensed at 85 °C with acidic EtOH solution (5 mL HCl per 100 mL EtOH) for reflux for 48 h. The further reaction products were collected and washed with anhydrous EtOH and deionized water three times, separately, to completely remove the templating agent CTAB. Finally, the synthesized products were dispersed in deionized water and freeze-dried using freezing desiccant to obtain MSNs.

Surface modification of MSNs was performed as described previously [41]. APTES was used as the silane coupling agent to react with the silanol group on the surface of MSNs and for successful branch coupling with amino groups. The synthesized MSNs were dispersed in 100 mL anhydrous MeOH added with 1 mL APTES. The MSNs were reflowed for 12 h under a boiling water bath, centrifuged, and washed. The final products were dispersed into deionized water. After freeze-drying, a white solid powder was obtained and named MSNs-NH_2. HAS was loaded into MSNs-NH_2 through the solvent-drying method. Briefly, 15 mg HAS and 50 mg MSNs-NH_2 were each dissolved separately in 10 mL acetone, and ultrasonication was performed for 10 min for homogenization. Then, the two solutions were mixed in a beaker, sealed, and stirred away from light for 12 h. Afterward, the beaker was opened to volatilize the solvent, and HAS would remain in the pores of the MSNs, thereby achieving drug-loading. To prevent HAS leakage from the MSN pores, the coarse product was washed several times with saturated HAS solution, washed three times with deionized water, and centrifuged. The collected HAS@MSNs-NH_2 was stored at 4 °C away from light. To achieve the targeting of drug-loaded nanoparticles, the surfaces of the nanoparticles were further modified with ATS, which can specifically bind to prohibitin on the surface of WAT cells. Briefly, 3 mg ATS was dissolved in 10 mL phosphate-buffered saline (PBS) buffer solution, and the mixture was subsequently added with 31.4 mg EDC and 57.54 mg NHS. The mixture was then placed on a magnetic agitator and stirred at room temperature for 15 min to activate the carboxyl groups in the peptides. Then, 20 mL PBS buffer suspension containing HAS@MSNs-NH_2 (1 mg/mL) was added, and the system was stirred at room temperature for 24 h. The final reaction products were washed repeatedly with deionized water to remove the unreacted EDC, NHS, and ATS peptides to obtain pure HAS@MSNs-ATS.

2.3 Characteristics of the MSNs

The particle size and zeta potential of the synthesized products were analyzed using an Anton Paar particle size analyzer (Graz, Austria). The characteristic absorption peaks of

the synthesized nanoparticles were explored by Fourier transform infrared spectrometry (FTIR; Nicolet iS20, Thermo-Fisher Scientific, Waltham, MA, USA) at 400–4000 cm^{-1}.

The surface structures and shapes of the prepared MSNs were analyzed by scanning electron microscopy (SEM). Briefly, the nanoparticle samples were glued directly to the conductive adhesive and coated with gold using a Quorum SC7620 sputtering coater (45 s, 10 mA) (Quorum Technologies Ltd., Laughton, UK). The morphology was observed and photographed using a Zeiss Sigma 300 SEM (Oberkochen, Germany) with a secondary electron (SE2) detector at an acceleration voltage of 3 kV. Furthermore, the interior structural characteristics of the prepared MSNs were determined under transmission electron microscopy (TEM). Briefly, the diluted MSN sample was deposited on the copper grid, coated with carbon, and observed and photographed under a JEOL JEM-2100 TEM (Tokyo, Japan).

Nitrogen adsorption–desorption assay was performed to analyze the specific surface area and pore volume of the prepared MSNs. Briefly, a 30-mg sample of MSNs was degassed at 150 °C for 12 h, after which nitrogen adsorption and desorption analysis was performed at 77 K liquid nitrogen atmosphere using an APSP 2460 four-stage automatic specific surface area analyzer (Micromeritics Instrument Co., Norcross, GA, USA). The isothermal adsorption and desorption curve was recorded, and the total specific surface area of the nanoparticles was calculated using the Brunauer–Emmett–Teller method.

2.4 Determination of polypeptide graft density on MSN surface

The successful modification of polypeptides was confirmed using the bovine serum albumin (BSA) method, and the polypeptide grafting rate was determined by thermogravimetric analysis using a Mettler TGA2 Thermal Gravimetric Analyzer (Zurich, Switzerland).

2.5 Calculation of encapsulation rate and drug-loading

To evaluate the drug-loading capacity and encapsulation rate of the MSNs, we investigated the drug-loading solution, drug-loading time, HAS content, and proportion of nanoparticles, and determined the optimal drug-loading nanoparticle preparation process. HAS@MSNs-ATS (10 mg) was dispersed in 10 mL methanol and extracted by ultrasonication for 30 min. After which, the mixture was closed-stirred at room temperature for 12 h with a magnetic stirrer. The samples were then extracted by ultrasonication for another 30 min after magnetic stirring. Finally, the supernatant was collected, and the HAS content of the supernatant was determined by high-performance liquid chromatography (HPLC) assay with HAS as the reference substance. Briefly, chromatographic separation was performed on an Agilent 1260 HPLC system (Agilent Technologies, Inc., Santa Clara, CA, USA) equipped with an Agilent Zorbax SB C_{18} column (150×4.6 mm; particle size, 5 μm) with an acetonitrile–water (40: 60) mobile phase at a flow rate of 1.0 mL/min under 270 nm. The encapsulation and HAS loading rates were calculated as reported previously with minor modifications [42]:

$$\text{Encapsulation rate}=M_1/M\times 100\%, \quad (1)$$

$$\text{Drug-loading rate}=M_1/M_2\times 100\%, \quad (2)$$

where M is the total amount of drug input, M_1 is the drug load in drug-carrying nanoparticles, and M_2 is the weight of drug-loaded nanoparticles.

2.6 In vitro biocompatibility testing of MSNs

The in vitro biocompatibility of drug-loaded nanoparticles was evaluated by hemolysis and protein binding rate testing. Fresh blood was collected from the Sprague-Dawley rats for hemolysis testing. Red blood cells were dispersed in Dulbecco's phosphate-buffered saline (DPBS). MSN samples with different concentrations (10–5000 μg/mL) were added and incubated at 37 °C for 1 h. Ultra-pure water (UPW) was used as the positive control and DPBS as the negative control. After incubation, the samples were centrifuged at 10 000*g* for 5 min, and the absorbance of the samples was measured at 540 nm. The hemolysis rates of the samples were calculated as follows:

$$\text{Hemolysis rate}=(OD_{MSNs}-OD_{DPBS})/(OD_{\text{ultra-pure water}}-OD_{DPBS})\times 100\%, \quad (3)$$

where OD represents the optical density (absorbance).

The nanoparticles were dispersed in BSA solution (1 mg/mL) and stirred at 37 °C for 24 h. Then, the supernatant was obtained by centrifugation, and the protein content was measured using a BCA assay kit. PBS was used as the negative control in the experiment. The following equation was used to calculate the protein binding rate of MSNs:

$$\text{Protein adsorption rate}=(M_{\text{BSA solution (1 mg/mL)}}-M_{\text{supernatant solution}})/M_{\text{BSA solution (1 mg/mL)}}\times 100\%, \quad (4)$$

where M represents the mass.

2.7 Stability evaluation of MSNs

HAS@MSNs-ATS (10 mg) was dispersed in 5 mL PBS buffer (pH 7.4) at a concentration of 2.0 mg/mL, and the mixture was placed at room temperature. The particle size and zeta potential values of HAS@MSNs-ATS particles were measured at 1, 2, 4, 6, 8, 10, and 12 d using an Anton Paar particle size meter.

2.8 Cytotoxicity

The 3T3-L1 cell line exhibits specificity for differentiation into adipocytes, which is the ideal cell model for investigating obesity and other fat metabolism-related diseases [34, 35]. Therefore, we used 3T3-L1 cells to evaluate the cytotoxicity of HAS-loaded nanoparticles. The 3T3-L1 pro-lipid cells (Guangzhou Cellcook Biotech Co., Guangzhou, China) were cultured in Dulbecco's modified Eagle medium (DMEM) containing 10% fetal bovine serum (FBS) and 1% penicillin-streptomycin with 5% CO_2 at 37 °C. The medium was replaced, and cell passage was performed every two days. Briefly, 3T3-L1 cells were seeded into 96-well plates and then treated with different concentrations of HAS@MSNs-NH_2 (5, 10, 20, 40, 60, 80, and 100 μg/mL) and HAS@MSNs-ATS (5, 10, 20, 40, 60, 80, and 100 μg/mL) for 12, 24, and 48 h. The CCK-8 kit was used to determine the cytotoxicity of HAS-loaded nanoparticles on 3T3-L1 cells.

2.9 Behaviors of drug-loaded MSNs in vitro

The release behaviors of drug-loaded particles in vitro were studied using the dialysis method. An 80:20 mixture of PBS (pH 7.4) and methanol was used as the dissolution medium. Then, 10 mg HAS@MSNs-NH_2 or 10 mg HAS@MSNs-ATS was dispersed in 3 mL dissolution medium. Furthermore, 3 mg HAS was dissolved in 10 μL DMSO, after which 3 mL dissolution medium was added. The three samples were placed in 150-kD dialysis bags, which were then placed in a beaker containing 100 mL dissolution medium. A magnetic stirrer was used to slowly stir the dissolution medium at 37 °C. After which, 1 mL liquid was collected from the beaker at 1, 2, 3, 4, 5, 6, 7 and 8 h. The same volume of blank dissolution medium was immediately added back to the mixture. The experiment was repeated three times. HPLC was performed as described earlier to determine the HAS content in the dissolution medium (M_1). The total amount of drug molecules released at different time points was calculated using the following equation:

$$\text{Cumulative release rate}=C_1/C_{\text{HAS}}\times 100\%, \quad (5)$$

where C_1 is the determined HAS contents in the dissolution medium and C_{HAS} is the loading HAS contents in nanoparticles. The results were used to plot the drug release curve.

2.10 Cell culture and treatment

In the induced differentiation experiment, 3T3-L1 cells were seeded into culture plates and cultured for 2 d. Then, induction medium 1 (containing 0.5 mmol/L 3-isobutyl-1-methylxanthine, 1 μmol/L dexamethasone (DEX), and 10 μg/mL insulin) was added, and the cells were cultured further for 2 d. Subsequently, induction solution 2 (10 μg/mL insulin) was added to replace induction medium 1, and the culture was continued for another 2 d. After 2-d culture, induction solution 2 was replaced completely with 10% FBS medium for further culture, and the medium was changed every two days. Ultimately, more than 90% of 3T3-L1 cells showed a mature adipocyte phenotype (including morphology and lipid accumulation, Fig. S1 in the supplementary information) after 8–12 d of differentiation [43]. For HAS treatment, HAS was added at the beginning of 3T3-L1 fusion until mature adipocytes were formed, while the control group was treated with a culture medium containing 0.5% DMSO. Cell viability was determined using the CCK-8 assay kit.

2.11 Uptake of nanosystems by 3T3-L1 cells

FITC was used to prepare FITC@MSNs-NH_2 and FITC@MSNs-ATS. Fluorescence intensity was measured using the luciferase assay to balance the amount of FITC in the two nanoparticle samples prior to treatment. The uptake of FITC@MSNs and FITC@MSNs-ATS by 3T3-L1 cells before and after differentiation was evaluated by laser confocal microscopy (Leica, Heidelberg, Germany). Briefly, undifferentiated 3T3-L1 cells and differentiated mature 3T3-L1 cells were inoculated into 6-well plates or laser confocal dishes. After the cells were fully adhered to the 6-well plates, a culture medium containing FITC@MSNs-NH_2 or FITC@MSNs-ATS was added, and the mixtures were incubated for 8 h. Then, the medium was discarded, and the cells were washed three times with PBS. The cells were collected, and fluorescence intensity was measured using a flow cytometer (BD FACSCelesta, Franklin Lakes, NJ, USA).

4',6-Diamidino-2-phenylindole (DAPI) staining and LysoTracker staining were performed to label the nuclei and lysosomes, respectively. Endocytosis of the nanoparticles was observed on laser confocal microscopy (Leica, Heidelberg, Germany). To elucidate the targetability of the drug delivery system, adipocytes were pretreated with free ATS peptide or endocytic blocker chloroquine prior to nanoparticle incubation. To study the time-dependent uptake of nanoparticles by mature 3T3-L1 adipocytes, lysosomes were stained with LysoTracker, and intracellular fluorescence changes were observed on confocal laser microscopy at different time points.

2.12 Obesity animal model and grouping

Male specific-pathogen-free C57BL/6L mice ((20±2) g) aged eight weeks were raised in a standard animal house with free access to water and food during the experiment. After one week of adaptive feeding, six mice were randomly selected for the normal control (NC) group, which continued feeding on an ordinary diet. The remaining mice were fed with a high-fat diet (HFD; 60% fat, 20% protein, and 20% carbohydrates) for 12 weeks. After 12 weeks, the weights of the mice were measured, and the whole-body fat of the mice

was analyzed by micro-computed tomography (CT) [44]. Obesity was defined as a weight gain over 20% compared with NC mice [45] and significant whole-body fat accumulation on micro-CT. Then, the obese mice were randomly divided into six groups (n=6): saline, HAS alone, MSNs-NH_2, MSNs-ATS, HAS@MSNs-NH_2, and HAS@MSNs-ATS groups. All drugs were dissolved in normal saline (for the HAS alone, approximately 3% DMSO was used to enhance solubility) and injected 200 μL via the caudal vein once every three days for 30 d. The HAS dosage in the HAS alone, HAS@MSNs-NH_2, and HAS@MSNs-ATS groups was administered at 2.5 mg/kg based on the results of preliminary experiments conducted before the formal investigation. The weight and food intake of the mice were calculated and recorded every three days.

2.13 Oral glucose and insulin tolerance testing

Obesity is often accompanied by insulin resistance and disorders in oral glucose tolerance and insulin tolerance [26, 44]. Therefore, before the end of the animal experiment, an oral glucose tolerance test (OGTT) and an insulin tolerance test (ITT) were performed in mice as described previously [46, 47]. Briefly, mice were fasted for 6 h and then administered with glucose (2.0 g/kg) or insulin (0.75 U/kg) by intraperitoneal (i.p.) injection. Then, blood samples were collected via the tail vein at 0 (before the injection), 15, 30, 60, 90, and 120 min after treatment. Blood glucose was measured using a commercial blood glucose meter with test strips (Roche, Basel, Swiss). After blood glucose values were recorded at each time point, the areas under the curve (AUCs) of OGTT and ITT were determined.

2.14 Cold exposure experiment

Cold exposure is commonly used to investigate the adaptive thermogenesis of animals in cold environments [26, 48]. Cold exposure experiment was performed as previously reported [26, 48]. Briefly, the anal temperature of mice was recorded as the basal body temperature at room temperature before cold exposure. The mice were then placed in a cold chamber at 4 °C, and anal temperature was determined at 30, 60, 90, and 120 min. Furthermore, the body surface temperature was measured using an infrared thermometer (FOTRIC 600C, Shanghai, China).

2.15 Micro-CT

Micro-CT is the ideal non-invasive method of evaluating the whole-body fat of animals, which can judge the nature of tissues based on CT values [26]. Fat quantitative analysis was performed by micro-CT (Bruker SkyScan, Seattle, WA, USA), and then fat parameters were measured and accurately combined with the rich post-processing algorithms of CTVol micro-CT software (Bruker SkyScan). Subsequently, a three-dimensional reconstruction of the fat in the bodies of the animals was performed, and CTAN software (Bruker SkyScan) was used for image analysis.

2.16 Collection of blood and tissue samples

One hour after the last drug administration, blood samples were collected from the abdominal artery under anesthetization (pentobarbital sodium, 45 mg/kg, i.p.). Subsequently, the mice were sacrificed, and tissue samples (liver, BAT, inguinal WAT [iWAT], epididymal WAT [eWAT], perirenal WAT [pWAT], and mesenteric WAT [mWAT]) were collected. Then, 5 mm×5 mm samples of the tissues were fixed in 4% paraformaldehyde for histopathological examinations. The remaining tissue specimens were frozen at −80 °C for subsequent biochemical analysis.

2.17 Biodistribution and targeting specificity of nanoparticles in mice

To verify the adipose targetability of the nanoparticle delivery system, DIR, a red fluorescent probe that stains the cell membrane, was used to synthesize DIR@MSNs-NH_2 and DIR@MSNs-ATS. On the day before the end of the animal experiment, three mice were randomly selected from the MSNs-NH_2 and MSNS-ATS groups and injected with 200 μL DIR@MSNs-NH_2 and DIR@MSNs-ATS (2 mg/kg DIR) via the tail vein (i.v.), respectively. The fluorescence intensity was measured using a fluorescence microplate reader (Varioskan LUX, ThermoFisher Scientific), and the DIR contents in the two particles were balanced. After 8 h, in vivo imaging was performed to determine the distribution of the nanoparticle drug delivery materials in mice using a PerkinElmer IVIS Spectrum imaging system (Waltham, MA, USA). Mice were sacrificed, and organs and adipose tissue were collected for fluorescence imaging.

2.18 Detection of biochemical indexes

The blood samples were left to stand at room temperature for 1 h and subsequently centrifuged for 10 min (4 °C, 3000 r/min) to isolate the serum. The serum levels of ALT, AST, TG, TC, low density lipoprotein cholesterol (LDL-C), and high density lipoprotein cholesterol (HDL-C) were measured using an automatic biochemical analyzer for animals (Mindray BS-240VET, Shenzhen, China).

2.19 Hematoxylin and eosin staining and oil red O staining

The fixed tissues were embedded in paraffin and stained with hematoxylin and eosin (H&E) to observe the pathological

changes in mouse tissues. Furthermore, frozen liver tissues were sliced into frozen sections and stained with oil red O as described previously [44] to observe the lipid accumulation in mouse liver tissues.

2.20 Cell mitochondrial stress test

3T3-L1 cells in the logarithmic growth stage were inoculated into Seahorse XFe24 well plates (Agilent Technologies, Inc.) and induced to differentiate into mature adipocytes [49]. During induction, HAS, HAS@MSNs-NH_2, or HAS@MSNs-ATS was added to be cultured with the cells. Cell mitochondrial respiration was analyzed using an Agilent XF24 Analyzer (Agilent Technologies, Inc.).

2.21 Detection of mitochondrial changes

3T3-L1 cells in the logarithmic growth stage were inoculated into 6-well plates or laser confocal dishes and induced to differentiate into mature adipocytes. HAS, HAS@MSNs-NH_2, or HAS@MSNs-ATS was added during induction. At the end of the experiment, the MitoTracker probe was used to dye the mitochondria of cells, and laser confocal microscopy was performed to observe the changes in the number of mitochondria. Flow cytometry was performed to analyze the MitoTracker-dyed mitochondria in 3T3-L1 cells. Untreated 3T3-L1 cells were used as the blank control. During induction, HAS, HAS@MSNs-NH_2, or HAS@MSNs-ATS was added, and the cell density was adjusted to 1×10^7 mL^{-1}. The MitoTracker probe was used to strain the mitochondria in 3T3-L1 cells and subsequently analyzed by using a flow cytometer (BD FACSCelesta, Franklin Lakes, NJ, USA). Mitochondria in the 3T3-L1 cells were analyzed under TEM (JEOL JEM-2100, Tokyo, Japan) as described previously [50, 51].

2.22 Western blotting assays

Mature adipose cells were treated with HAS, HAS@MSNs-NH_2, or HAS@MSNs-ATS nanoparticles. The cells were harvested, and cell proteins were extracted to prepare the total protein content. After quantification using BCA kits, equal amounts of total proteins (30 μg) were loaded into a sodium dodecyl sulfate/polyacrylamide gel electrophoresis (SDS/PAGE) kit to separate the targeting protein bands. After separation, the targeting protein bands were transferred to a polyvinylidene fluoride (PVDF) membrane and subsequently incubated with the corresponding primary and secondary antibodies. ECL reagents were used to visualize the targeting protein bands. β-actin was used as the internal reference for normalizing protein loading. Protein expression was quantified as a value relative to that of β-actin [44, 52].

2.23 Calcium ion concentration in cell detection

3T3-L1 cells in the logarithmic growth stage were inoculated into 6-well plates or laser confocal dishes and induced to differentiate into mature adipocytes. HAS, HAS@MSNs-NH_2, or HAS@MSNs-ATS was added during induction. The rhod-2 AM probe was incubated with the cells for 30 min. The cells were collected, and the changes in calcium ion concentration were observed under flow cytometry and laser confocal microscopy [44].

2.24 Safety of targeted drug delivery systems

HAS alone, HAS@MSNs-NH_2, and HAS@MSNs-ATS were administered at 2.5 mg/kg once every three days for 30 d. After which, blood samples were collected into a centrifuge tube containing heparin sodium, and the numbers of red blood cells and white blood cells were determined using an automatic blood biochemical detector (Mindray BC-2800VET, Shenzhen, China) to evaluate the safety of the nanoparticle drug delivery system in vivo. The liver, heart, spleen, lungs, and kidneys of mice were harvested, fixed in paraformaldehyde, and stained with H&E for histopathological examination according to a previously described method.

2.25 Data analysis

All experimental results were expressed as mean±standard deviation (SD), and GraphPad Prism 8.00 software (San Diego, CA, USA) was used to draw illustrations. Statistical analysis was performed using SPSS 20.0 software (Chicago, IL, USA). One-way analysis of variance was performed, followed by Dunnet *t* multiple comparisons test to compare between different groups. $P<0.05$ was considered statistically significant.

3 Results and discussion

3.1 Synthesis process optimization of MSNs

To obtain MSNs with an appropriate particle size, the EtOH ratio (%), temperature (°C), and the ratio of CTAB (g) to TEOS (mL) were investigated to optimize the MSN synthesis process. The ideal MSNs would have a small particle size (approximately 100 nm), high zeta potential (positive or negative), and small polymer dispersity index (PDI). A higher zeta potential (positive or negative) indicates higher electrostatic repulsion and better stability. PDI is a key parameter used to describe the uniformity of particle size distribution. A smaller PDI value means a more uniform particle size distribution. Therefore, based on our preliminary experiments before the formal investigation, single-factor analysis was used

to investigate the optimized parameters for particle size, zeta potential, and PDI values. Based on the evaluation indexes of particle size, zeta potential, and PDI values of the synthesized particles, the optimal parameters for the synthesis of MSNs were finally determined as follows: an EtOH ratio of 10%, synthesis temperature of 85 °C, and CTAB (g):TEOS (mL)= 1:6 (Table S1 in the supplementary information). The synthesized MSNs have a relatively uniform particle size distribution of approximately 100 nm.

3.2 Characterization of HAS@MSNs-ATS nanoparticles

The particle size of nanoparticles did not change significantly after amino modification but increased slightly following peptide modification; nevertheless, the particle size remained at approximately 120 nm ((128.84±5.45) nm; PDI=12.49%; Fig. 2a and Table S2 in the supplementary information). The mean zeta potential of MSNs was −36.54 mV due to the presence of the silicon hydroxyl group on the surface but increased to +30.67 mV after amino modification (PDI= 10.30%), indicating that the amino group was successfully coupled to the MSN surface. However, the surface potential of the nanoparticle decreased to +10.47 mV after polypeptide modification (Fig. 2b and Table S2 in the supplementary information). SEM revealed that the synthesized MSNs were spheroidal and uniformly dispersed with a uniform particle size of approximately 100 nm, which was consistent with the particle size measured using the laser particle size analyzer (Fig. 2c). TEM revealed that after the removal of the templating agent CTAB, honeycomb and orderly holes were formed on the surface of the silicon sphere, indicating that CTAB decomposed into volatile gas at high temperatures, which facilitated particle loading for HAS (Fig. 2d). The infrared spectra of MSNs-CTAB showed prominent absorption peaks at 1470, 2854, and 2925 cm^{-1}. However, these peaks disappeared in the MSN spectra, indicating that

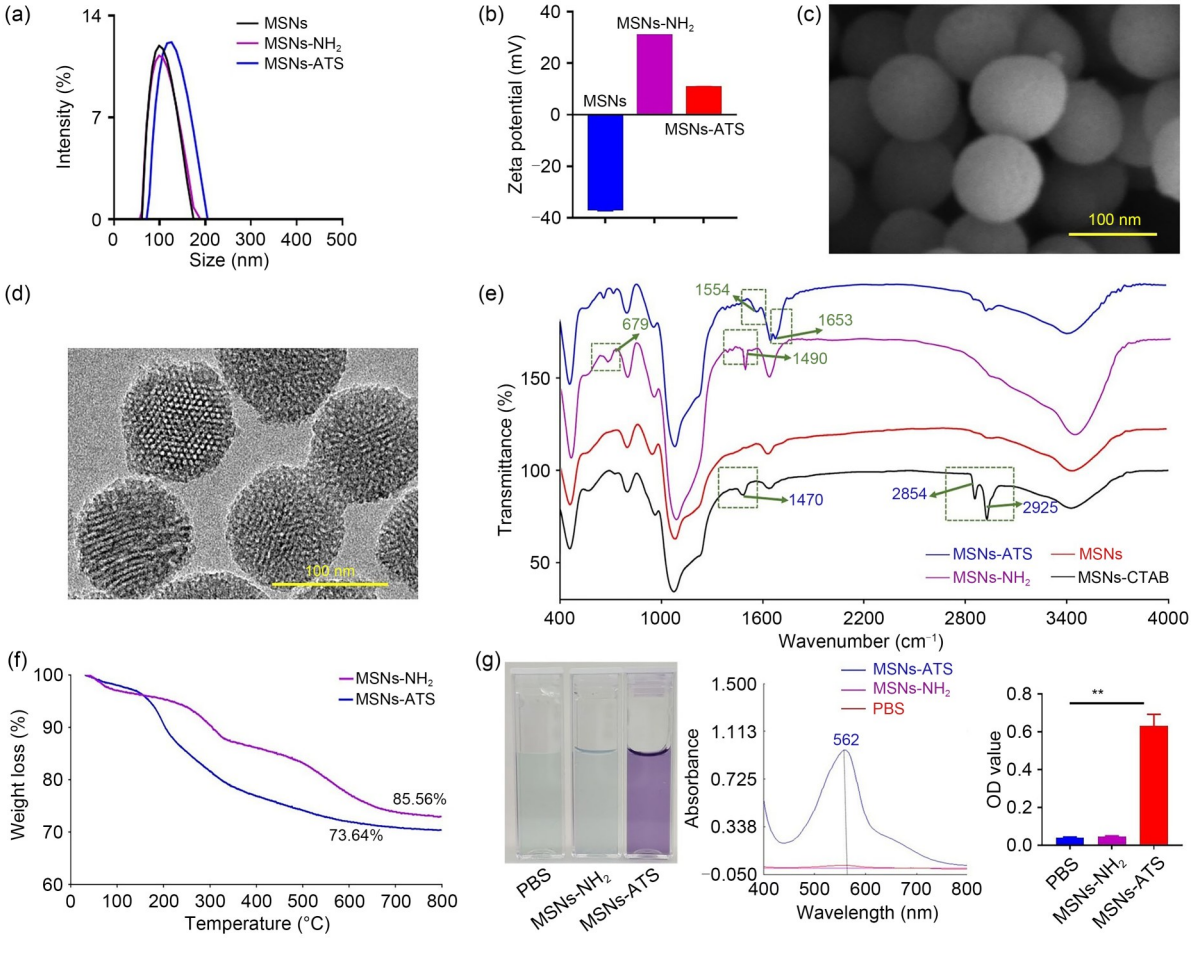

Fig. 2 Characterization of HAS-loaded nanoparticles: (a) size of MSNs, MSNs-NH_2, and MSNs-ATS; (b) zeta potential of MSNs, MSNs-NH_2, and MSNs-ATS; (c, d) scanning and projection electron microscopy images of MSNs; (e) Fourier infrared results of MSNs; (f) thermogravimetric analysis curves of MSNs-NH_2 and MSNs-ATS; (g) results of BCA assay of MSNs-ATS. Data are expressed as mean±standard deviation (n=3). $^{**}p<0.01$, vs. MSNs-ATS. HAS: hydroxy-α-sanshool; MSN: mesoporous silica nanoparticle; ATS: adipose-targeting sequence; BCA: bioinchoninic acid; PBS: phosphate-buffered saline; OD: optical density

CTAB was successfully removed from the MSNs. Furthermore, compared with the MSNs, MSNs-NH_2 exhibited characteristic absorption peaks at 1490 and 679 cm^{-1} in the infrared spectrum, which were bending vibration peaks of two amino N-H bonds, indicating the successful amino modification of the MSNs. In addition, the comparison of the nanoparticle spectra before and after peptide linking showed that the bending vibration absorption peaks of the amino group weakened after the peptide linking, and the characteristic peaks of the I and II bands at 1653 and 1554 cm^{-1} amide appeared, indicating that the target peptide ATS was successfully linked to the surface of the MSNs (Fig. 2e). Thermogravimetric analysis (TGA) revealed that the ratio of ATS modification on the MSNs-ATS surface was approximately 11.92% (Fig. 2f). In addition, a purple color reaction occurred between MSNs-ATS and BCA working solution, with the solution showing a strong UV absorption peak at 562 nm, which further confirmed the presence of polypeptides on the surface of the MSNs (Fig. 2g). The N_2 adsorption–desorption isotherm curves and parameter changes of the nanoparticles before and after peptide modification further indicated that ATS was successfully adhered to the surface of the MSNs (Fig. S2 in the supplementary information).

The drug-loading process was assessed based on the encapsulation rate and drug-loading capacity. The final drug-loading process was determined as follows: acetone was the drug-loading solvent, the drug-loading time was 12 h, and the feeding ratio was 3:7 (Table S3 in the supplementary information). The drug-loading of HAS@MSNs-ATS was (83.72±1.08)%, and the encapsulation rate was (26.40±0.25)% (Table S3 in the supplementary information).

HAS alone at room temperature could not dissolve in PBS; however, HAS@MSNs-NH_2 and HAS@MSNs-ATS containing the same amount of HAS became translucent in PBS, turning milky white, indicating that the loading of nanoparticles greatly improved the water solubility of HAS (Fig. 3a). Similarly, HAS@MSNs-ATS ((127.32±4.50) nm, +9.54 mV; PDI=13.251%) has a slightly larger particle size than HAS@MSNs-NH_2 ((110.53±2.39) nm, +31.69 mV; PDI=10.303%) and a lower potential due to the presence of surface peptides (Figs. 3b and 3c). The physical stability of HAS@MSNs-ATS in different solutions was also investigated (Fig. 3d). The particle size of HAS@MSNs-ATS remained almost unchanged in PBS and DMSO within 12 days, indicating the good stability of MSNs-ATS. The in vitro biocompatibility of drug-loaded nanoparticles was evaluated by hemolysis and protein binding experiments. HAS@MSNs-NH_2 had very low hemolysis and protein binding rates, whereas HAS@MSNs-ATS basically did not exhibit hemolysis but showed a decreased protein binding rate, indicating good in vitro biocompatibility. Thus, polypeptide modification can further enhance the biocompatibility of MSNs (Figs. 3e and 3f).

3.3 In vitro drug release of HAS-loaded MSNs

The release behavior of HAS alone, HAS@MSNs-NH_2, and HAS@MSNs-ATS in vitro was explored by dialysis. As shown in Fig. 3g, all HAS samples showed high release rates within 8 h. The release rate of HAS alone was 83.98% at 2 h, with complete release achieved at 8 h, whereas those of HAS@MSNs-NH_2 and HAS@MSNs-ATS were 39.05% and 30.58% at 2 h, respectively. The release rates of HAS@MSNs-NH_2 and HAS@MSNs-ATS at 8 h were 74.56% and 68.81%, respectively, which were significantly lower than that of HAS alone. Meanwhile, at 24 h, the release rates of HAS@MSNs-NH_2 and HAS@MSNs-ATS were 92.63% and 88.43%, respectively, indicating that the release of HAS could be delayed by the MSN system. We also found that the drug release curves of HAS@MSNs-NH_2 and HAS@MSNs-ATS gradually flattened over time, and no significant difference was observed between the two. Thus, HAS@MSNs-NH_2 and HAS@MSNs-ATS could stably and slowly release their drug loads. Furthermore, the peptide modification of the MSN surface did not affect drug release. Fitting of the in vitro release data revealed that the release behavior of HAS alone was consistent with the first-order kinetic model with an R^2 of 0.9706. The release behaviors of HAS@MSNs-NH_2 and HAS@MSNs-ATS were consistent with the first-order kinetic model, with R^2 of 0.9946 and 0.9925, respectively (Table S4 in the supplementary information).

3.4 Cytotoxicity of HAS-loaded MSNs

Figures 3h and 3i present the effects of HAS@MSNs-NH_2 and HAS@MSNs-ATS on the viability of 3T3-L1 cells, respectively. HAS@MSNs-NH_2 showed no obvious cytotoxic effects on cell viability within 12 h, and the cell viability was higher than 90%. However, the cell viability gradually decreased with increasing treatment time. When HAS@MSNs-NH_2 concentration >20 μg/mL, the viability of 3T3-L1 cells was decreased at 24 and 48 h (cell viability <90%). Similarly, the viability of cells treated with 5–100 μg/mL HAS@MSNs-ATS for 12 h showed no obvious cytotoxic effects (cell viability >90%) but decreased gradually with increasing treatment time. However, the viability of 3T3-L1 cells was not affected at HAS@MSNs-ATS concentration <40 μg/mL, whether the treatment time was 24 h or 48 h. The results indicate that ATS modification of the HAS@MSNs particles can reduce the cytotoxicity of drug-loaded MSNs.

3.5 In vitro targetability of ATS-modified MSNs

In vitro targeting of the MSNs-ATS system was investigated using FITC@MSNs-NH_2 and FITC@MSNs-ATS (Figs. 4a–4c). The binding capacities of undifferentiated 3T3-L1 cells to FITC@MSNs-NH_2 and FITC@MSNs-ATS within 8 h were comparable. However, the binding of FITC@MSNs-ATS

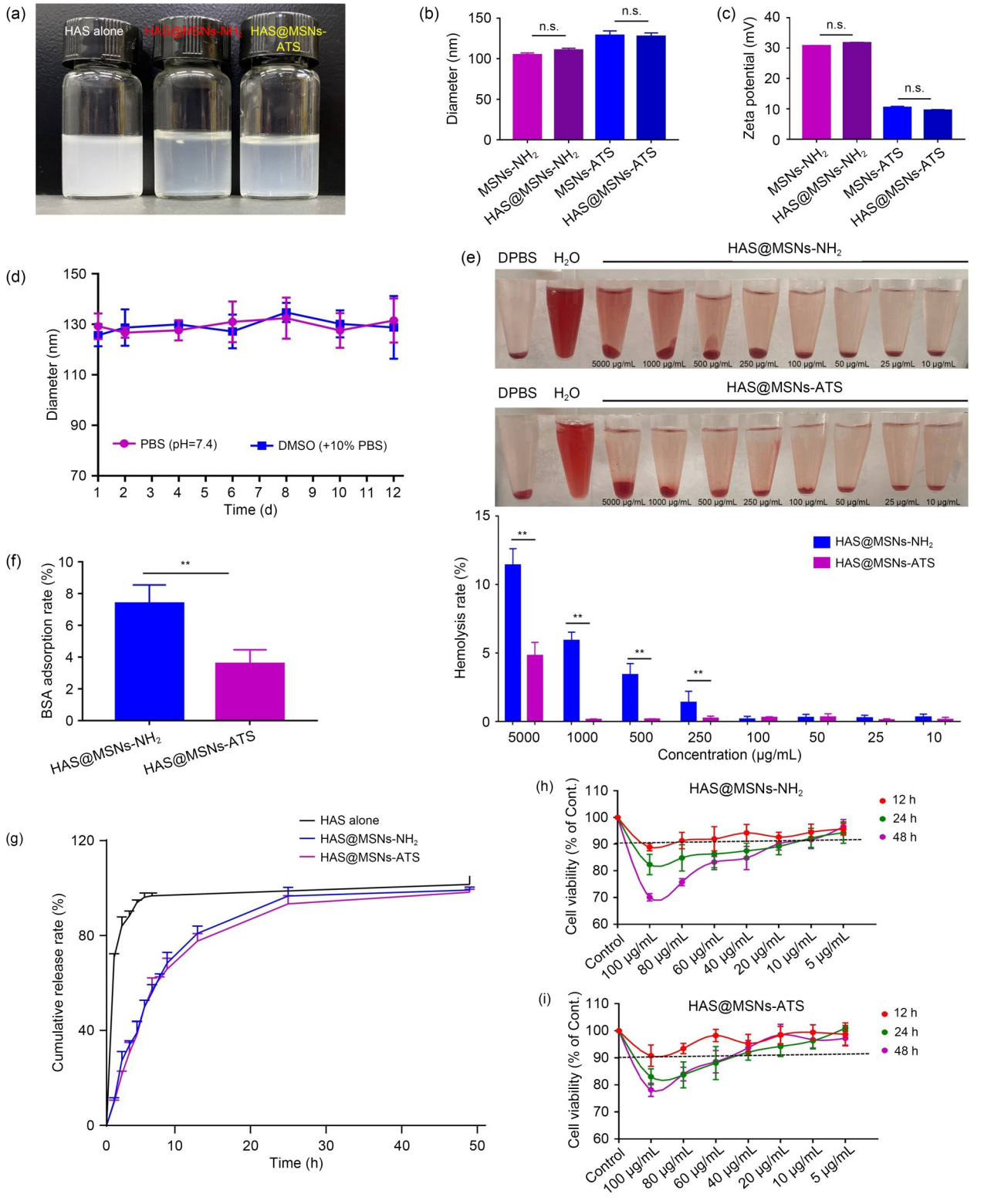

Fig. 3 In vitro release and safety of HAS-loaded nanoparticles: (a) different nanoparticles dissolved in PBS; (b) changes in the particle size of drug-carrying nanoparticles; (c) changes in the zeta potential of drug-carrying nanoparticles; (d) stability test results of HAS@ MSNs-ATS; (e) hemolysis test results of HAS@MSNs-NH_2 and HAS@MSNs-ATS at different concentrations; (f) protein binding rates of HAS@ MSNs-NH_2 and HAS@MSNs-ATS; (g) in vitro release curves of HAS alone, HAS@MSNs-NH_2, and HAS@MSNs-ATS; (h, i) effects of different concentrations of HAS@MSNs-NH_2 and HAS@MSNs-ATS on the viability of 3T3-L1 cells at 12, 24, and 48 h. Data are expressed as mean±standard deviation (n=3). $^{**}p$<0.01; n.s., not significant. HAS: hydroxy-α-sanshool; MSN: mesoporous silica nanoparticle; ATS: adipose-targeting sequence; PBS: phosphate-buffered saline; DMSO: dimethyl sulfoxide; BSA: bovine serum albumin

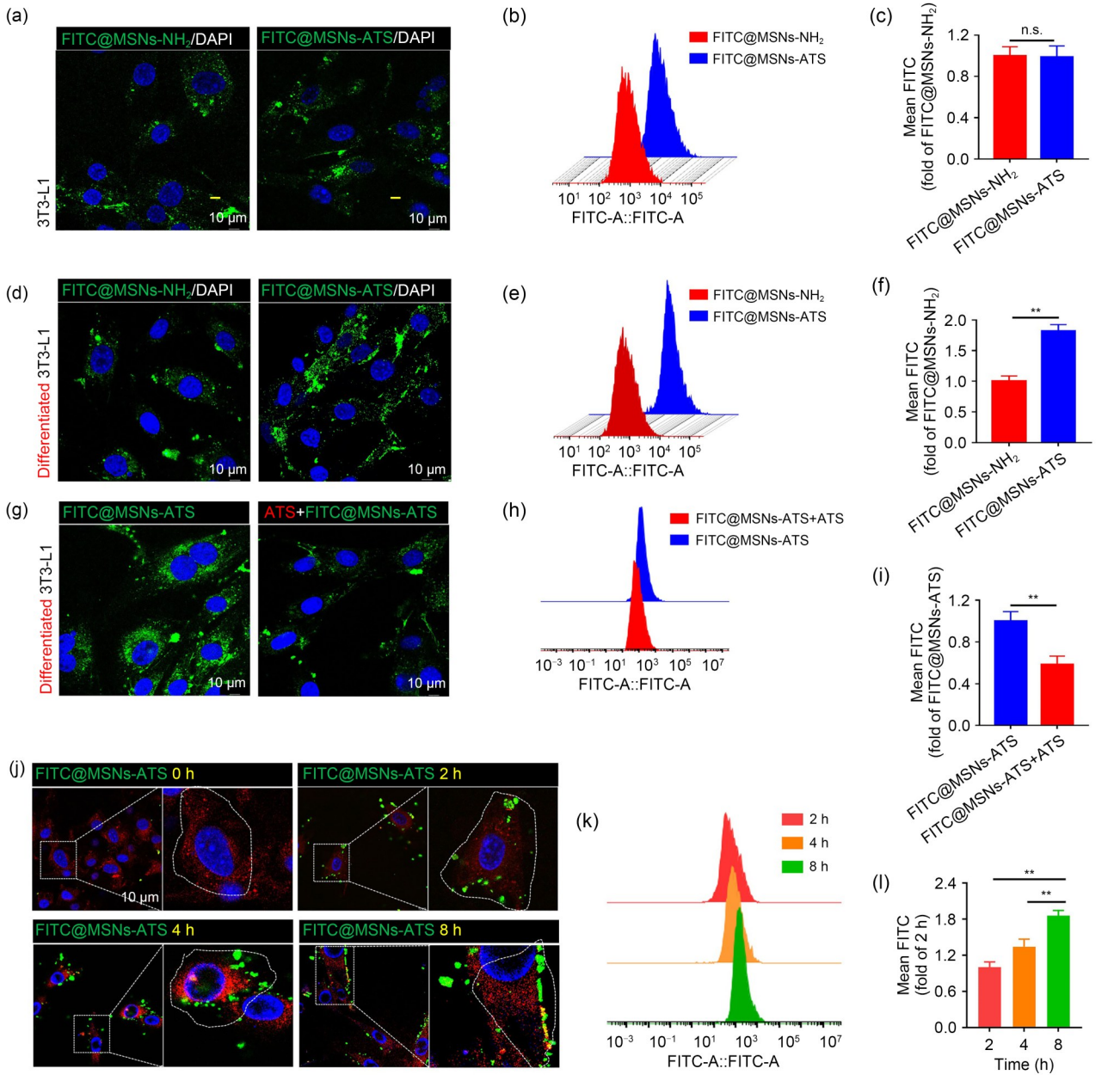

Fig. 4 Mature adipose cells bind specifically to FITC@MSNs-ATS. (a–f) FITC@MSNs-NH_2 and FITC@MSNs-ATS bind to cell membranes in vitro (green fluorescence, FITC-marked MSNs; blue fluorescence, DAPI-marked cell nuclei). Data are expressed as mean±SD (n=3). $^{**}p$<0.01, vs. FITC@MSNs-NH_2; n.s., not significant. (g–i) Effects of ATS preconditioning on the binding ability of FITC@ MSNs-ATS in mature 3T3-L1 cells (green fluorescence, FITC-marked MSNs; blue fluorescence, DAPI-marked cell nuclei; red fluorescence, LysoTracker-marked lysosome). Data are expressed as mean±SD (n=3). $^{**}p$<0.01, vs. FITC@MSNs-ATS. (j–l) Time-dependent uptake of FITC@MSNs-ATS by differentiated 3T3-L1 cells. Data are expressed as mean±SD (n=3). $^{**}p$<0.01, vs. FITC@MSNs-ATS uptake of cells after 8 h treatment. FITC: fluorescein isothiocyanate; MSN: mesoporous silica nanoparticle; ATS: adipose-targeting sequence; DAPI: 4′,6-diamidino-2-phenylindole; SD: standard deviation

by mature 3T3-L1 cells was higher than that of FITC@MSNs-NH_2 (p<0.01), because the classical "cocktail" therapy can induce 3T3-L1 preadipocytes to differentiate into mature adipocytes. ATS on the surface of FITC@MSNs-ATS nanoparticles specifically bound to the prohibitin on the adipocyte surface (Figs. 4d–4f). Similarly, the binding of FITC@MSNs-ATS by mature 3T3-L1 cells was higher than that by undifferentiated 3T3-L1 cells, implying that adipocyte binding of MSNs-ATS is receptor-mediated. Confocal microscopy revealed that preconditioning mature adipocytes with free ATS reduced the binding capacity of FITC@MSNs-ATS by adipocytes. Similarly, flow cytometry showed the decreased binding of FITC@MSNs-ATS by adipocytes pretreated with ATS (p<0.01) (Figs. 4g–4i).

3.6 Uptake of HAS-loaded MSNs by differentiated 3T3-L1 cells

The fluorescence and flow cytometry results in Fig. 4j show that numerous FITC@MSNs-ATS were bound to the membrane of the cells after co-incubation for 2 h, which increased after 4 h of treatment. Furthermore, the number of cell-bound nanoparticles gradually increased with time, indicating that fat cells could bind nanoparticles in a time-dependent manner (Figs. 4j–4l). To further demonstrate the targetability of ATS-modified MSNs to adipocytes, the HAS contents of adipocytes treated with HAS@MSNs-NH_2 and HAS@MSNs-ATS were determined. The HAS content of the cells treated with HAS@MSNs-ATS was 1.6 times that of cells treated with HAS@MSNs-NH_2 (Fig. S3 in the supplementary information), which was consistent with the fluorescence and flow cytometry results (p<0.01). Therefore, our ATS-modified MSNs could promote the absorption of drug delivery particles by adipocytes.

3.7 In vivo targetability of ATS-modified MSNs

Different DIR-labeled nanocarriers were injected into mice through the caudal vein, and their distribution was observed using an imaging system for small animals in vivo. As shown in Fig. 5a, ATS-modified DIR@MSNs showed more fluorescence accumulation in the iWAT, eWAT, and pWAT of obese mice. Fluorescence studies of isolated adipose tissue (Figs. 5b–5i), revealed that the fluorescence signal of DIR was the highest in iWAT (Figs. 5f and 5g). Meanwhile, the fluorescence intensity of the iWAT of the DIR@MSNs-ATS–treated mice was 1.9 times higher than that of mice treated with DIR@ MSNs-NH_2 (Fig. 5g, p<0.01). Furthermore, the intensity of the DIR signal in the livers of mice treated with

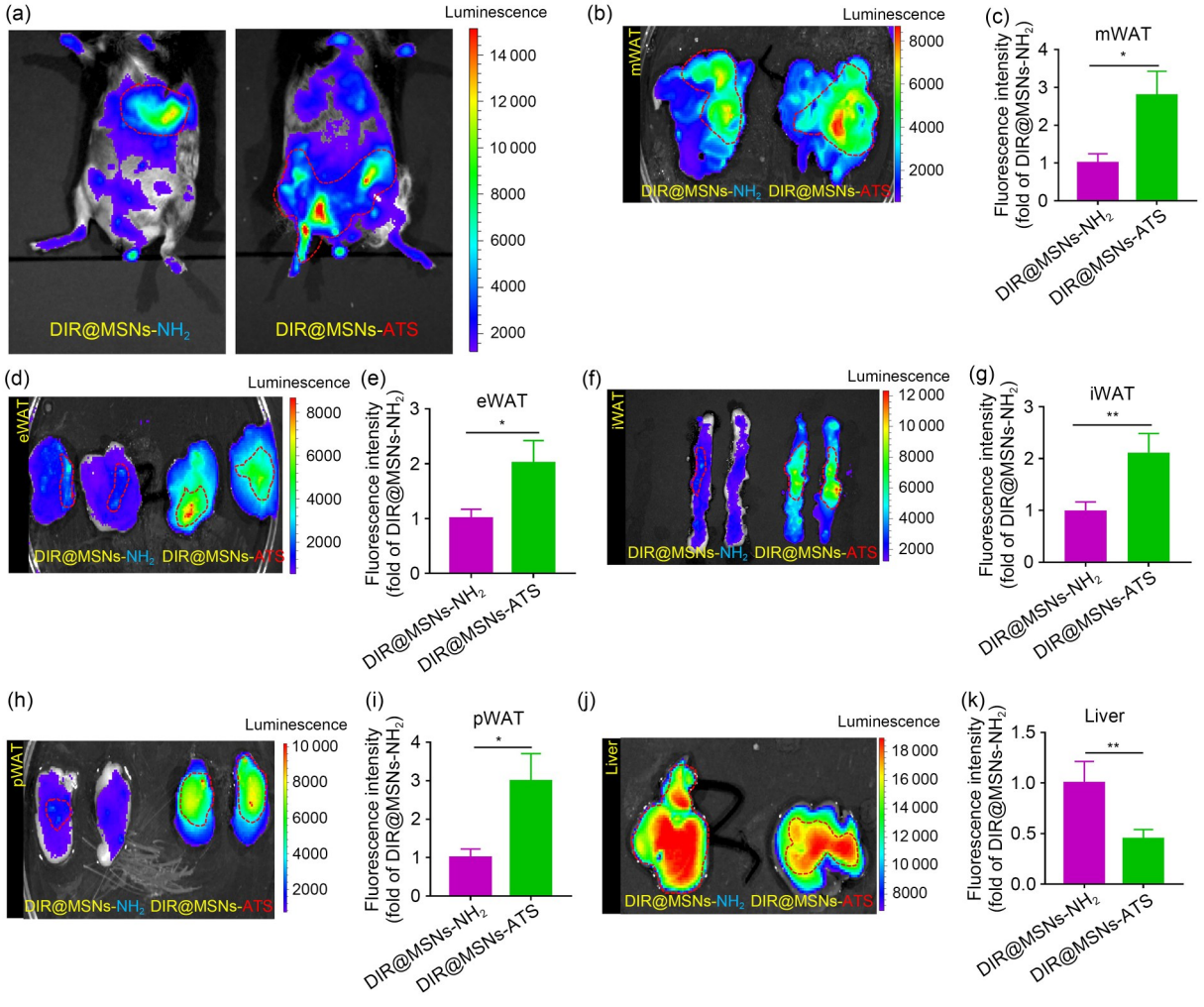

Fig. 5 Adipose targetability of HAS-loaded nanoparticles. (a) An in vivo imaging instrument was used to observe the distribution of nanocarriers in small animals; (b–k) Fluorescence statistics of the distribution of nanocarriers in mWAT, eWAT, iWAT, pWAT, and liver of mouse. Data are expressed as mean±standard deviation (n=3), $^{*}p$<0.05 and $^{**}p$<0.01, vs. DIR@MSNs-NH_2. HAS: hydroxy-α-sanshool; WAT: white adipose tissue; mWAT: mesenteric WAT; eWAT: epididymal WAT; iWAT: inguinal WAT; pWAT: perirenal WAT; DIR: 1,1-dioctadecyl-3,3,3,3-tetramethylindotricarbocyaine iodide; ATS: adipose-targeting sequence

DIR@MSNs-ATS was 55.21% lower than in those treated with DIR@MSNs-NH_2 (Figs. 5j and 5k). These data show that DIR@MSNs-ATS can target WAT in obese mice, specifically the iWAT.

3.8 HAS-loaded MSNs promoted body weight reduction

Weight reduction is the most intuitive index for evaluating the effects of candidate drugs on obesity. Weight changes in mice were also recorded in the present study. On the 27th day of treatment, the weight of mice in the HAS group decreased (Fig. 6a). Similarly, HAS-loaded MSNs reduced the body weight in obese mice. However, on Day 24, the body weight of mice in the HAS@MSNs-NH_2 group was lower than that in the saline group (Fig. 6a). Interestingly, on the last day of the experiment, mice in the HAS@MSNs-NH_2 group weighed less than those treated with HAS alone (Fig. 6a). We speculated that MSN loading promoted the weight reduction effect of HAS. In addition, compared with obese mice treated with normal saline, HAS-loaded MSNs-ATS treatment significantly reduced weight on Day 21 (Fig. 6b) to gradually approach the weight of mice fed a normal diet. At the end of the experiment, the body weight of the mice treated with HAS@MSNs-ATS was lower than those treated with HAS alone and HAS@MSNs-NH_2 ($p<0.05$) (Fig. 6c) despite no significant differences in food intake (Fig. 6d). These results demonstrate that MSN loading and ATS peptide modification can significantly increase the anti-obesity effects of HAS. This may be because peptide modification can directly target drug delivery to the adipocytes.

As shown in Fig. 6e, after 12 weeks on HFD, the mice showed obvious signs of obesity, with a large amount of abdominal fat accumulation and heavier weight than the NC group. The evaluation of the anti-obesity effects of HAS also included the MSNs and MSNs-ATS groups to avoid the influence of excipients on the body weight of mice. Compared with mice treated with normal saline, the MSNs had no effect on body weight or abdominal fat accumulation in mice. Similar to the effect of HAS alone, HAS-loaded MSNs reduced fat accumulation, with HAS@MSNs-ATS exhibiting a more remarkable effect on fat reduction (Fig. 6e). Importantly, the HAS alone and HAS-loaded MSNs had no effect on the food intake of mice, indicating that the weight reduction effect of HAS and HAS-loaded MSNs did not induce appetite reduction (Fig. 6d).

3.9 HAS-loaded MSNs improved serum biochemical indexes

Serum samples were collected at the end of the mentioned animal experiment, and analyzed for biochemical indexes. As shown in Figs. 6f–6i and Fig. S4 (supplementary information), HFD did not significantly increase serum AST but increased serum ALT in obese mice ($p<0.05$), indicating that liver injury may be associated with obesity. Furthermore, HFD can increase the serum levels of TG ($p<0.05$), TC ($p<0.05$), and LDL-C ($p<0.05$). However, the levels of ALT, TG, TC, and LDL-C under treatment with HAS alone and HAS-loaded MSNs decreased ($p<0.05$), indicating that HAS and HAS-MSNs can improve the liver injury and lipid levels associated with obesity. Importantly, the results indicated that MSN loading and ATS modification increased the effects of HAS on serum biochemical indexes. Our results also showed that MSNs alone did not significantly affect serum biochemical indexes (Fig. 6).

3.10 HAS-loaded MSNs improved liver fat accumulation

As shown in Figs. 6j–6m, HFD caused serious fat accumulation in the liver of obese mice as shown by H&E staining. Large fat vacuoles were formed in the liver of obese mice, and pathological phenomena observed included necrosis of liver cells, accumulation of fat droplets, and interstitial edema (Fig. 6l). Oil red O staining also revealed numerous fat droplets in the liver of obese mice (Fig. 6m). Treatment with HAS alone, HAS@MSNs-NH_2, and HAS@MSNs-ATS reduced and/or improved liver lesions, fat droplets, hepatocyte necrosis, and interstitial edema, with a higher improvement observed under the MSN treatments than under HAS alone. In particular, the liver cells in the HAS@MSNs-ATS group were compact and orderly, with a clear morphology and fewer fat droplets. Mouse livers were also observed and weighed. Compared with that of NC mice, the liver weight of obese mice increased (Figs. 6j and 6k). However, liver weight decreased after treatment with HAS, HAS@MSNs-NH_2, or HAS@MSNs-ATS ($p<0.05$). Subsequently, we calculated the liver index of mice and found no significant changes in any of the groups (Fig. 6k). Furthermore, MSNs and MSNs-ATS did not affect the liver weight or organ index (Figs. 6j and 6k), and did not affect the liver steatosis in obese mice (Figs. 6l and 6m).

3.11 HAS-loaded MSNs improved insulin resistance

Obesity often causes insulin resistance [51]. In the present study, OGTT and ITT assays were performed to evaluate the effects of HAS and HAS-MSNs on insulin resistance in HFD-induced obese mice (Figs. 6n–6q). The OGTT assay revealed that the blood sugar levels in all mice increased after glucose administration but gradually decreased with time (Fig. 6n). The ITT assay revealed that after intraperitoneal injection of insulin, the blood sugar levels in all mice decreased but gradually recovered with time (Fig. 6p). The

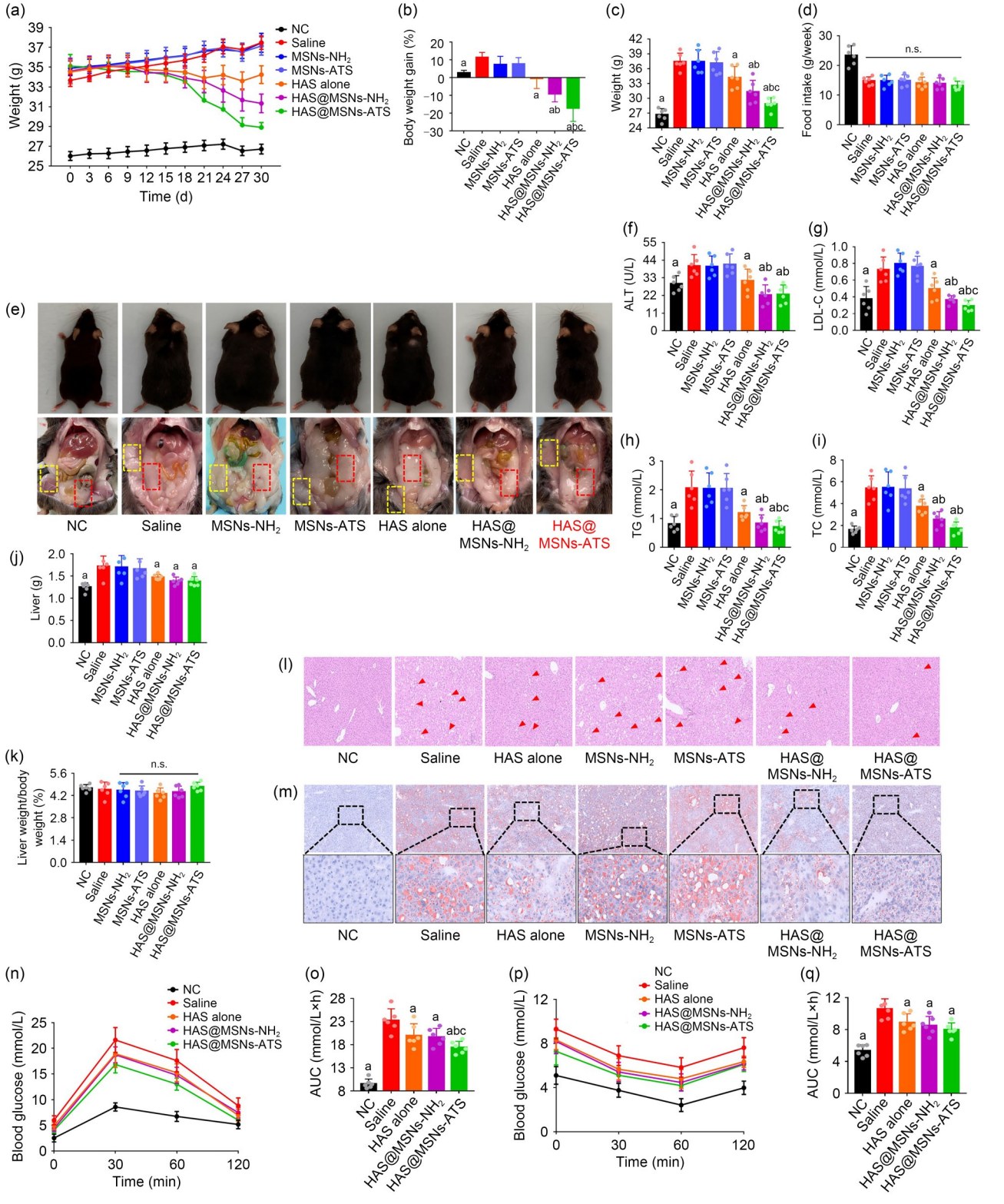

Fig. 6 MSNs-ATS nanoparticle system increased the anti-obesity effect of HAS. (a–d) Effects of drug-loaded nanoparticles on body weight and feed intake of obese mice. (e) Effects of drug-loaded nanoparticles on abdominal fat accumulation in obese mice. (f–i) Effects of nanoparticles on serum biochemical levels in obese mice. (j–m) Effects of nanoparticles on the liver of obese mice. (n, o) Effects of nanoparticles on glucose tolerance in obese mice. (p, q) Effects of nanoparticles on insulin tolerance in obese mice. Data are expressed as mean±standard deviation (n=6). [a]p<0.05, vs. saline (HFD mice treated with saline); [b]p<0.05, vs. HAS alone; [c]p<0.05, vs. HAS@MSNs-NH_2. n.s., not significant. MSN: mesoporous silica nanoparticle; ATS: adipose-targeting sequence; HAS: hydroxy-α-sanshool; HFD: high-fat diet; ALT: alanine aminotransferase; LDL-C: low density lipoprotein cholesterol; TG: triglycerides; TC: total cholesterol; AUC: area under the curve

AUCs of blood glucose changes, glucose tolerance (Fig. 6o), and insulin tolerance (Fig. 6q) of obese mice were higher than those of NC mice ($p<0.05$), indicating that obesity can cause impaired blood glucose regulation. The OGTT and ITT were improved by treatment with HAS, HAS@MSNs-NH_2, and HAS@MSNs-ATS ($p<0.05$). We further observed that HAS@MSNs-ATS caused more significant improvements on OGTT and ITT than HAS alone in obese mice ($p<0.05$).

3.12 HAS-loaded MSNs reduced body fat volume

The whole-body fat of mice was analyzed and reconstructed by micro-CT (Fig. 7). Compared with mice under a normal diet, HFD mice exhibited significant accumulation of total body fat, including subcutaneous WAT (sWAT; yellow color in Fig. 7) and visceral WAT (vWAT; green color in Fig. 7) ($p<0.05$). In addition, micro-CT analysis revealed that HFD feeding did not affect BAT (red color in Fig. 7). Interestingly, our results indicated that treatment with HAS and HAS-MSNs (HAS@MSNs-NH_2 and HAS@MSNs-ATS) alleviated this pathological phenomenon ($p<0.05$). In addition, HAS-loaded MSNs significantly alleviated fat accumulation in sWAT better than HAS alone ($p<0.05$).

After drug intervention, eWAT, pWAT, mWAT, iWAT, and BAT of mice were collected and weighed (Figs. 8a–8m). Similar to the results of micro-CT analysis, the weights of eWAT, pWAT, mWAT, and iWAT from obese mice treated with saline were increased ($p<0.05$). The ratio of fat weight to body weight also increased ($p<0.05$). Treatment with HAS and HAS-MSNs (HAS@MSNs-NH_2 and HAS@MSNs-ATS) reduced the weight of these fat tissues ($p<0.05$) and the ratio of fat weight to body weight ($p<0.05$). Interestingly, the anti-obesity effects of HAS@MSNs-NH_2 and HAS@MSNs-ATS were higher than that of HAS alone ($p<0.05$). In addition, although the untreated obese mice had the largest BAT, the ratio of BAT to body weight was not different significantly from those of the other groups (Figs. 8j and 8k).

3.13 HAS-loaded MSNs reduced adipocyte volume

CT and anatomical observation revealed that HAS@MSNs-NH_2 and HAS@MSNs-ATS reduced fat accumulation in sWAT of obese mice. Pathological examination of the iWAT of mice was visualized by H&E staining (Figs. 8n–8p). Compared with the obese mice treated with saline, HAS alone and HAS-MSNs (HAS@MSNs-NH_2 and HAS@MSNs-ATS) reduced the iWAT volume ($p<0.05$). In addition, the adipocytes

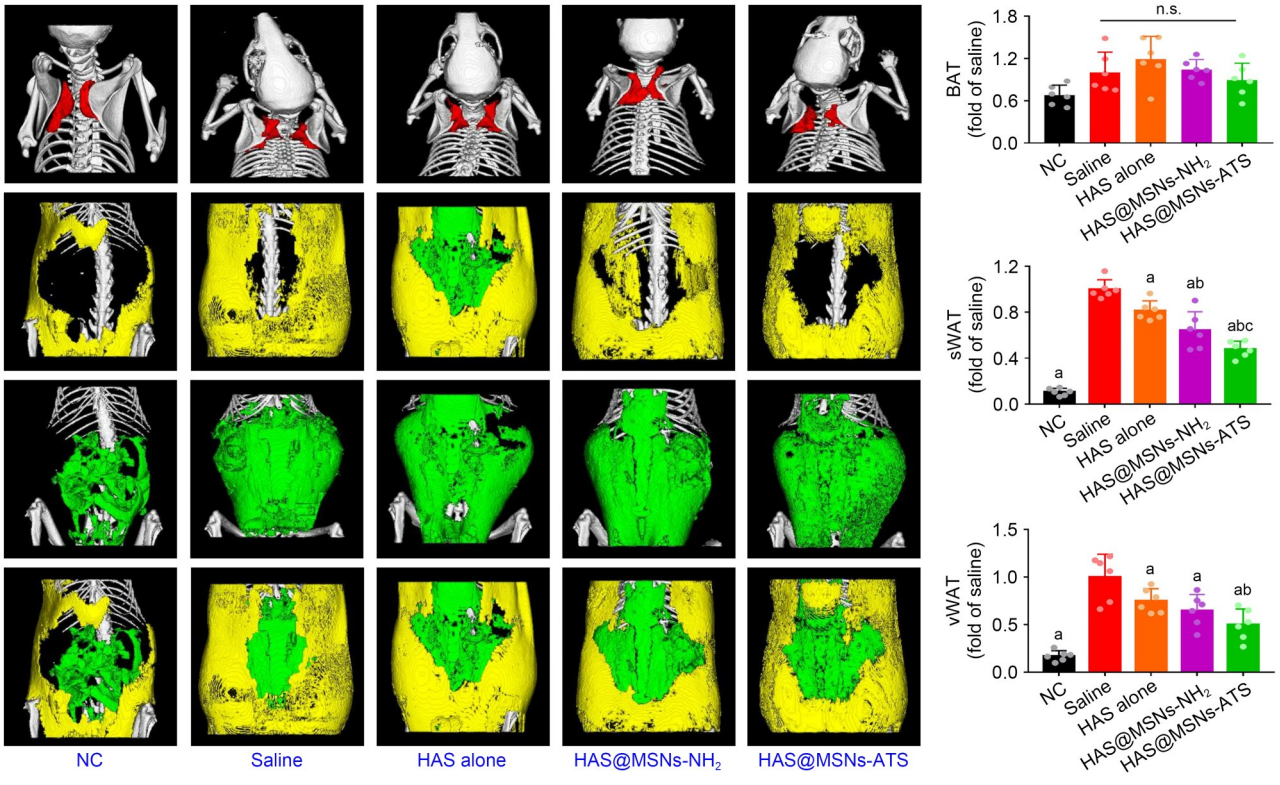

Fig. 7 Micro-computed tomography analysis showing the effects of nanoparticles on the total body fat volume of obese mice (yellow, sWAT; green, vWAT; red, BAT). Data are expressed as mean±standard deviation ($n=6$). [a]$p<0.05$, vs. saline (HFD mice treated with saline); [b]$p<0.05$, vs. HAS alone; [c]$p<0.05$, vs. HAS@MSNs-NH_2; n.s., not significant. WAT: white adipose tissue; BAT: brown adipose tissue; sWAT: subcutaneous WAT; vWAT: visceral WAT; HAS: hydroxy-α-sanshool; MSN: mesoporous silica nanoparticle; HFD: high-fat diet; ATS: adipose-targeting sequence

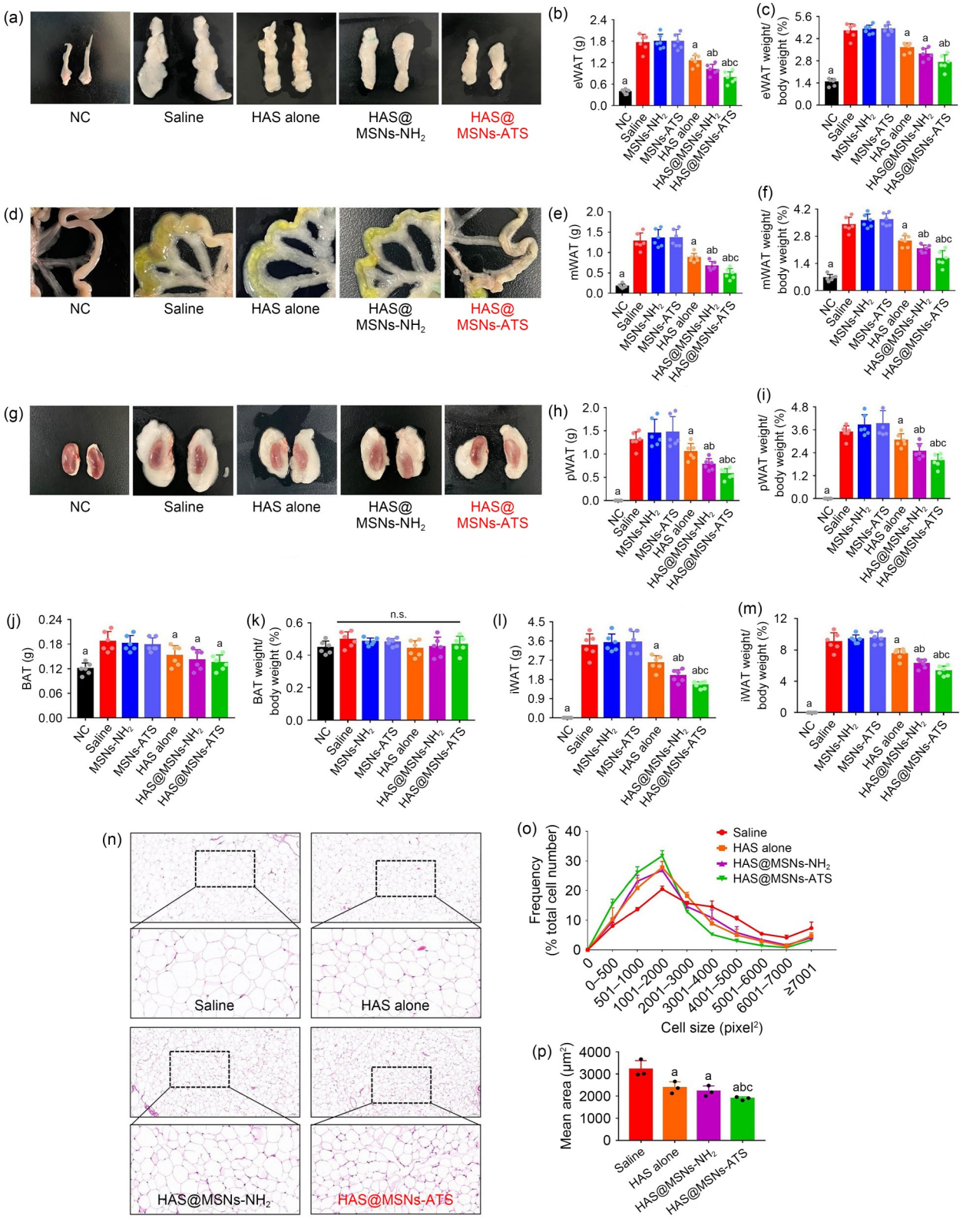

Fig. 8 HAS-loaded nanoparticles reduced the total body fat accumulation and adipocyte volume in obese mice. (a–m) Effects of HAS and its nanoparticles on eWAT, mWAT, pWAT, BAT, and iWAT in obese mice. (n–p) Effects of HAS and its nanoparticles on subcutaneous adipocyte volume in obese mice. Data are expressed as mean±standard deviation (n=6 for (b, c, e, f, h–m); n=3 for (o, p)). [a]p<0.05, vs. saline (HFD mice treated with saline); [b]p<0.05, vs. HAS alone; [c]p<0.05, vs. HAS@MSNs-NH_2; n.s.: not significant. HAS: hydroxy-α-sanshool; WAT: white adipose tissue; BAT: brown adipose tissue; iWAT: inguinal WAT; eWAT: epididymal WAT; pWAT: perirenal WAT; mWAT: mesenteric WAT; HFD: high-fat diet; MSN: mesoporous silica nanoparticle; ATS: adipose-targeting sequence

from mice treated with HAS@MSNs-NH_2 and HAS@MSNs-ATS were smaller than those treated with HAS (p<0.05). Furthermore, the adipocytes from mice treated with HAS@ MSNs-ATS showed an obvious multicompartment lipid droplet morphology, which is typical of brown and beige adipocytes.

3.14 HAS-loaded MSNs increased adaptive thermogenesis in obese mice

Reducing food intake or increasing energy expenditure can reverse obesity. In the present study, drug intervention had no significant effect on the food intake of mice, which indicates that HAS alone and HAS-MSNs (HAS@MSNs-NH_2 and HAS@MSNs-ATS) may decrease body weight by increasing energy consumption. The browning of WAT is an effective means of increasing the body's energy consumption, and the body's adaptive heat production is a sign of the browning of WAT. A cold exposure test was conducted to evaluate the effects of HAS alone, HAS@MSNs-NH_2, and HAS@MSNs-ATS on adaptive thermogenesis and browning of WAT in obese mice. Before the experiment, the anal temperature of mice was measured as basal body temperature (Fig. 9). Treatment with HAS alone and HAS-MSNs increased the basal body temperature, indicating that HAS could increase the resting heat production, with a more pronounced effect under treatment with HAS@MSNs-ATS (p< 0.05, HAS@MSNs-ATS vs. saline, Fig. 9a). After cold exposure at 4 °C, the thermoregulation ability of mice treated with HAS and HAS-MSNs was higher than that of control mice, indicating that the MSN encapsulation and peptide modification of HAS did not reduce its efficacy. The temperature change curve showed that the HAS@MSNs-NH_2 and HAS@MSNs-ATS groups exhibited better thermoregulation ability (Fig. 9b). After treatment at 4 °C for 180 min, the body temperature of mice in the administration group was higher than that in the control group. The body temperature in the HAS@MSNs-ATS group was higher than that in the HAS alone group (p<0.05, HAS@MSNs-ATS vs. HAS alone, Fig. 9c). Similar results were obtained by infrared thermal imaging (Fig. 9d). For 180 min at 4 °C, the body surface temperature of mice in the drug administration group was higher than that of the control group. Thus, HAS-MSNs promoted adaptive thermogenesis in obese mice, with a more pronounced effect with the ATS-modified MSNs.

3.15 HAS-loaded MSNs promoted the adipocyte browning in obese mice

Mitochondria are the centers of cell energy metabolism [53, 54]. The effects of HAS and HAS-MSNs on mitochondrial oxygen consumption in adipocytes were studied using the mitochondrial pressure assay (Figs. 10a–10e). Compared with HAS monotherapy, HAS@MSNs-NH_2 and HAS@MSNs-ATS treatments showed higher oxygen consumption rates for basal respiration, proton respiration, maximal respiration, and spare respiratory capacity of mature 3T3-L1 cells (p<0.05).

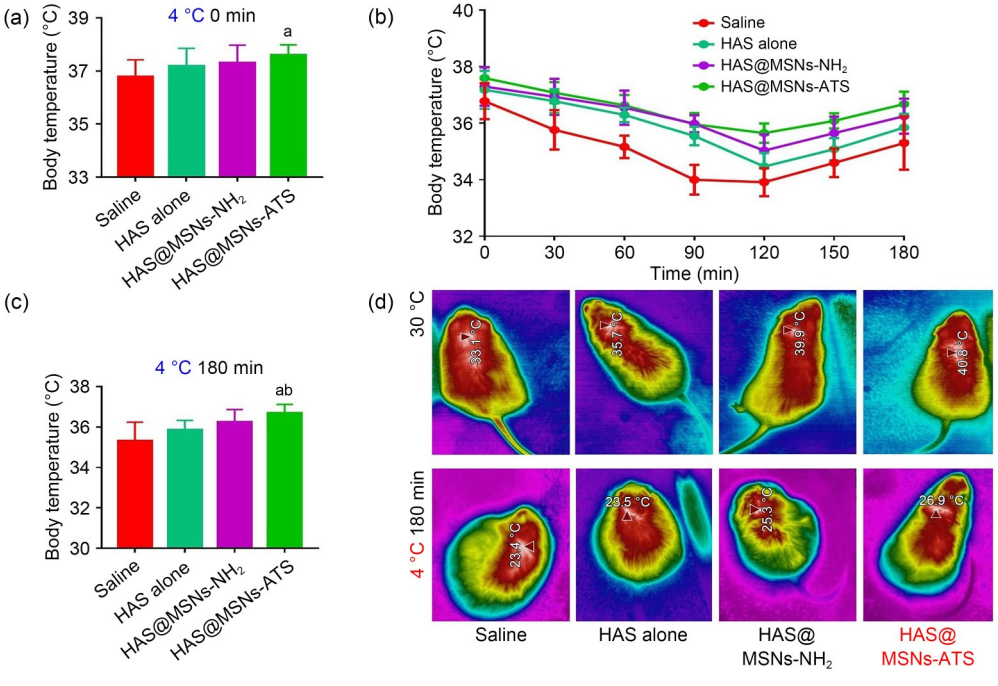

Fig. 9 HAS-loaded MSNs increased adaptive thermogenesis in obese mice. The body temperature of mice at 4 °C for 0 min (a), within 180 min (b), and after 180 min (c). (d) Thermal imaging of mice at 4 °C. Data are expressed as mean±standard deviation (n=6). [a]p<0.05, vs. saline (HFD mice treated with saline); [b]p<0.05, vs. HAS alone; [c]p<0.05, vs. HAS@MSNs-NH_2. HAS: hydroxy-α-sanshool; MSN: mesoporous silica nanoparticle; HFD: high-fat diet; ATS: adipose-targeting sequence

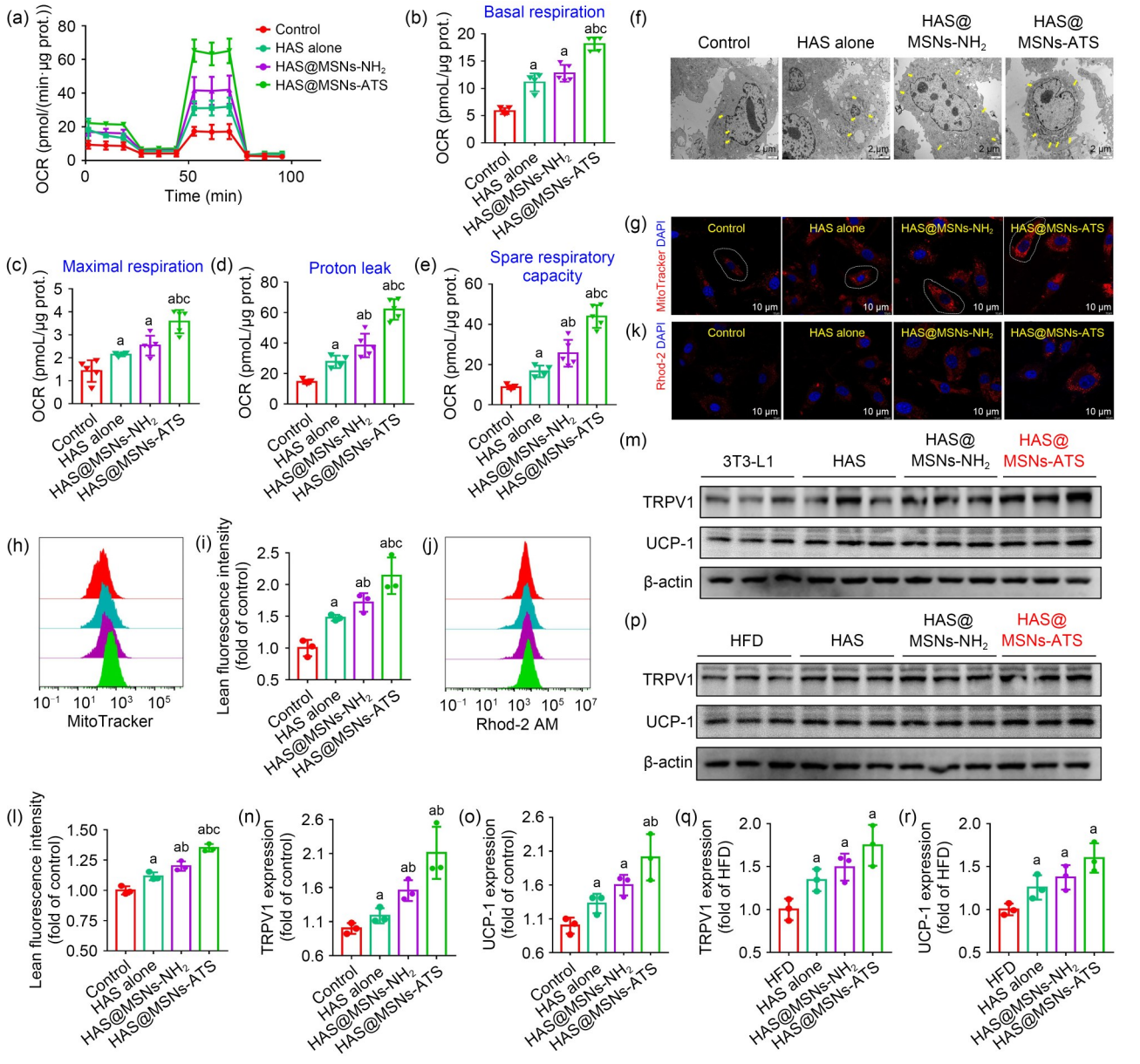

Fig. 10 HAS and its nanoparticles induced adipocyte browning. (a–e) Effects of HAS and its nanoparticles on mitochondrial pressure in adipocytes. Data are expressed as mean±SD (n=5). ^{a}p<0.05, vs. control; ^{b}p<0.05, vs. HAS alone; ^{c}p<0.05, vs. HAS@MSNs-NH_2. (f–i) Effects of HAS and its nanoparticles on the number of mitochondria in adipocytes (red fluorescence, MitoTracker marked mitochondria; blue fluorescence, DAPI-marked cell nuclei). Data are expressed as mean±SD (n=3). ^{a}p<0.05, vs. control; ^{b}p<0.05, vs. HAS alone; ^{c}p<0.05, vs. HAS@MSNs-NH_2. (j–l) Effects of HAS and its nanoparticles on calcium influx in adipocytes (red fluorescence, rhod-2-marked calcium; blue fluorescence, DAPI-stained cell nuclei). Data are expressed as mean±SD (n=3). ^{a}p<0.05, vs. control; ^{b}p<0.05, vs. HAS alone; ^{c}p<0.05, vs. HAS@MSNs-NH_2. (m–o) Effects of HAS and its nanoparticles on the expression of TRPV1 and UCP1 in adipocytes. Data are expressed as mean±SD (n=3). ^{a}p<0.05, vs. control; ^{b}p<0.05, vs. HAS alone; ^{c}p<0.05, vs. HAS@MSNs-NH_2. (p–r) Effects of HAS and its nanoparticles on the expression of TRPV1 and UCP1 in iWAT of obese mice. Data are expressed as mean±SD (n=3), ^{a}p<0.05, vs. HFD; ^{b}p<0.05, vs. HAS alone; ^{c}p<0.05, vs. HAS@MSNs-NH_2. OCR: oxygen consumption rate; WAT: white adipose tissue; HAS: hydroxy-α-sanshool; MSN: mesoporous silica nanoparticle; ATS: adipose-targeting sequence; SD: standard deviation; DAPI: 4′,6-diamidino-2-phenylindole; TRPV1: transient receptor potential vanilloid 1; UCP-1: uncoupling protein 1; rhod-2 AM: rhod-2 acetoxymethyl ester

Furthermore, the increased number of mitochondria is a typical indicator of adipocyte browning [55]. Therefore, the changes in the number of mitochondria in mature adipocytes were observed on TEM, laser confocal microscopy, and flow cytometry analysis. As shown in Figs. 10f–10i, the number of mitochondria in 3T3-L1 cells increased with HAS monotherapy (p<0.05). Importantly, compared with HAS monotherapy, treatments with HAS@MSNs-NH_2 and HAS@MSNs-ATS further increased the number of mitochondria in the cells (p<0.05).

In our previous study, we found that HAS can upregulate UCP-1 to trigger the browning of WAT by activating the TRPV1 and AMPK/SIRT1/PPAR-γ pathways [26]. Calcium influx results from TRPV1 channel activation and was thus investigated in the present study. Figures 10j–10l showed that, compared with the control group, HAS and HAS-MSNs increased calcium influx in mature 3T3-L1 cells ($p<0.05$). In the present study, we also investigated the effects of HAS-loaded nanoparticles on the expression of TRPV1 and UCP-1 in adipocytes. As shown in Figs. 10m–10o, HAS upregulated TRPV1 expression and increased UCP-1 production (which is also an indicator of WAT browning [26]) in mature 3T3-L1 cells. Compared with HAS monotherapy, treatment with HAS@MSNs-NH_2 further increased the TRPV1 and UCP-1 expression in cells ($p<0.05$). Furthermore, the calcium influx in cells treated with HAS@MSNs-NH_2 and HAS@MSNs-ATS was higher than those treated with HAS alone ($p<0.05$). Furthermore, HAS@MSNs-ATS had the strongest ability to increase calcium influx in mature 3T3-L1 cells. These results indicated that the HAS-loaded adipose-targeted drug delivery system can enhance the HAS-induced activation of TRPV1 expression in adipocytes. To further verify the in vivo WAT browning effect of the HAS-loaded nanoparticles, UCP-1 expressions in iWAT were investigated. As shown in Figs. 10p–10r, UCP-1 expression in iWAT of obese mice treated with HAS alone, HAS@MSNs-NH_2, and HAS@MSNs-ATS was 1.33, 1.60, and 2.01 times higher than in the iWAT of mice treated with normal saline, respectively. In addition, HAS and HAS-MSNs upregulated the expression of TRPV1 in iWAT, indicating that ATS-modified MSNs can deliver HAS targeted to iWAT and promote WAT browning.

Furthermore, the possible in vivo toxicities of HAS@MSNs-NH_2 and HAS@MSNs-ATS in heart, spleen, lung, liver, and kidney tissues were evaluated by histopathological examination with H&E staining. As shown in Fig. S5 (supplementary information), no significant pathological changes were observed in heart, spleen, lung, and kidney tissues between mice treated with HAS@MSNs-NH_2 or HAS@MSNs-ATS and saline-treated mice ($p>0.05$). HAS@MSNs-NH_2 and HAS@MSNs-ATS also reduced the lesions and lipid deposition in liver tissues without inducing toxicity (Figs. 6l and 6m). Furthermore, analysis of blood cells at the end of the experiment (Fig. S5 in the supplementary information) revealed that neither HAS alone nor HAS-MSNs showed adverse effects on the blood cells of mice.

4 Conclusions

Naturally occurring therapeutic agents, such as monomers or extracts from herbal medicines, are considered as important materials for the development of novel drugs used for the management of various diseases [56–58]. However, many such agents have poor druggability and therefore cannot exert adequate therapeutical effects in vivo. However, increasing evidence indicates that nanoparticle drug delivery systems with versatile abilities can increase the stability, controllability, bioavailability, and targetability of the loading drug [59, 60]. In 2001, a survey first described the use of MSNs as novel drug delivery materials for loading ibuprofen [58]. This drug delivery nanomaterial exhibited a high drug-loading capacity and exerted a sustained-release effect. Since then, MSNs have gained considerable attention as drug delivery systems [30–33]. Prohibitin is commonly highly expressed on the cell membrane of mature adipocytes. The short peptide ATS (sequence CKGGRAKDC) can specifically bind to prohibitin, which can increase the adipocyte targetability of nano-drug delivery systems [34, 35]. Browning for the WAT is a very effective mechanism for reversing obesity. Our previous study demonstrated the potential of HAS as a potential natural agent for inducing the browning of WAT. However, the solubility of HAS in water is very low, and HAS easily undergoes configuration transformation and oxidative degradation [27]. In the present study, we enhanced the stability and targetability of HAS by developing an @MSNs-ATS nano-drug delivery system for loading HAS. Furthermore, the in vitro mature 3T3-L1 cell model and in vivo obese mouse model were constructed to evaluate the adipocyte targetability, therapeutic efficacy, and toxicity of the HAS-loaded MSNs-ATS.

Improved targetability is a crucial goal in the development of novel drug delivery systems. The present study demonstrated that ATS-modified MSNs showed higher adipocyte targetability than pure MSNs in HFD-induced obese mice. The improved targetability may enhance the therapeutic efficacy of the loading drug [60]. Both the in vitro and in vivo results of our study indicated that HAS-loaded MSNs-ATS showed a higher therapeutic efficacy against obesity by triggering adipocyte browning than HAS alone. HAS-loaded MSNs-ATS can also increase adaptive thermogenesis in obese mice, the number of mitochondria in cells, calcium influx, and protein expression of UCP-1 and TRPV1 in adipocyte cells. Interestingly, HAS@MSNs-ATS exhibited more pronounced effects than HAS alone. Our evaluation of the safety of the HAS-loaded MSNs indicated that HAS alone and HAS-loaded MSNs showed high safety in liver, heart, kidney, lung, and spleen tissues, as well as whole blood cells, in mice.

However, our study has some limitations. Only male animals were used to avoid estrogen interference; therefore, more comprehensive experiments should be performed to explore the anti-obesity effects of HAS@MSNs-ATS in both male and female animals. Furthermore, the release behavior of HAS-loaded MSNs in vitro was studied using the dialysis method. The dialysis method is commonly used to determine

the in vitro release of drugs loaded in nanoparticles [61]. However, the dialysis tubing may delay the release of the loading drug. Consequently, other methods of determining the in vitro release of HAS-loaded MSNs-ATS, such as the flow-through cell method [62], should be performed in future investigations. Furthermore, only preclinical laboratory experiments were performed in the present investigation. Thus, further assessments of the therapeutic potential of HAS@MSNs-ATS against obesity must be conducted as clinical trials.

In summary, we successfully developed an adipose-targeted HAS-loaded MSN drug delivery system. Our in vivo and in vitro results indicated that HAS@MSNs-ATS can execute the targeted delivery of the loading drug to the adipocyte with good safety and anti-obesity effects.

Supplementary Information The online version contains supplementary material available at https://doi.org/10.1631/bdm.2400248.

Acknowledgements The authors thank Jiayi Sun (Innovative Institute of Chinese Medicine and Pharmacy, Chengdu University of Traditional Chinese Medicine, Chengdu, China) for his technological assistance in fluorescence microscope and flow cytometry analysis. This work was supported by the Natural Science Foundation of Sichuan Province (No. 2022NSFSC0720), Research Center for the Development of the Comprehensive Health Industry and Rural Revitalization of Sichuan TCM (No. DJKYB202306), and State Administration of Traditional Chinese Medicine of Sichuan Province of China (No. 2020HJZX001).

Author contributions QZ: formal analysis, investigation, methodology, writing—original draft. CXH: investigation, data curation, software, validation. JG: investigation, data curation, software. DDT: formal analysis, investigation. DQ: investigation, supervision, visualization. CZ: conceptualization, supervision, visualization. CJW: conceptualization, supervision, validation. WP: conceptualization, methodology, funding acquisition, writing—review & editing.

Declarations

Conflict of interest The authors declare that they have no known competing financial interests or personal relationships that could have appeared to influence the work reported in this paper.

Ethical approval All the animal use protocols were approved by the Experimental Animal Ethics Committee of Chengdu University of Traditional Chinese Medicine (Approval No. 2020-27).

Data availability Data will be made available on request.

References

1. Cheng YQ, Han JM, Li QH et al (2022) Metabolic obesity phenotypes: a friend or foe of digestive polyps?—An observational study based on national inpatient database. Metabolism 132:155201. https://doi.org/10.1016/j.metabol.2022.155201
2. Shi QY, Wang Y, Hao QK et al (2022) Pharmacotherapy for adults with overweight and obesity: a systematic review and network meta-analysis of randomized controlled trials. Lancet 399(10321):259–269. https://doi.org/10.1016/S0140-6736(21)01640-8
3. Zhang X, Zhang M, Zhao ZP et al (2020) Geographic variation in prevalence of adult obesity in China: results from the 2013–2014 national chronic disease and risk factor surveillance. Ann Int Med 172(4):291–293. https://doi.org/10.7326/M19-0477
4. Hales CM, Carroll MD, Fryar CD et al (2017) Prevalence of obesity among adults and youth: United States, 2015–2016. NCHS Data Brief 288:1–8
5. Elagizi A, Kachur S, Carbone S et al (2020) A review of obesity, physical activity, and cardiovascular disease. Curr Obes Rep 9(4): 571–581. https://doi.org/10.1007/s13679-020-00403-z
6. Goktas Z, Owens S, Boylan M et al (2013) Associations between tissue visfatin/nicotinamide, phosphoribosyltransferase (Nampt), retinol binding protein-4, and vaspin concentrations and insulin resistance in morbidly obese subjects. Mediators Inflamm 2013: 861496. https://doi.org/10.1155/2013/861496
7. Xu LY, Zhao WJ, Wang DM et al (2018) Chinese medicine in the battle against obesity and metabolic diseases. Front Physiol 9:850. https://doi.org/10.3389/fphys.2018.00850
8. Chakhtoura M, Haber R, Ghezzawi M et al (2023) Pharmacotherapy of obesity: an update on the available medications and drugs under investigation. EClinicalMedicine 58:101882. https://doi.org/10.1016/j.eclinm.2023.101882
9. Garvey WT, Ryan DH, Look M et al (2012) Two-year sustained weight loss and metabolic benefits with controlled-release phentermine/topiramate in obese and overweight adults (SEQUEL): a randomized, placebo-controlled, phase 3 extension study. Am J Clin Nutr 95(2):297–308. https://doi.org/10.3945/ajcn.111.024927
10. Khera R, Murad MH, Chandar AK et al (2016) Association of pharmacological treatments for obesity with weight loss and adverse events: a systematic review and meta-analysis. JAMA 315(22): 2424–2434. https://doi.org/10.1001/jama.2016.7602
11. Kwon YJ, Kwon GE, Lee HS et al (2022) The effect of orlistat on sterol metabolism in obese patients. Front Endocrinol 13:824269. https://doi.org/10.3389/fendo.2022.824269
12. Jobanputra R, Sargeant JA, Almaqhawi A et al (2023) The effects of weight-lowering pharmacotherapies on physical activity, function and fitness: a systematic review and meta-analysis of randomized controlled trials. Obes Rev 24(4):e13553. https://doi.org/10.1111/obr.13553
13. Baskaran P, Krishnan V, Ren J et al (2016) Capsaicin induces browning of white adipose tissue and counters obesity by activating TRPV1 channel-dependent mechanisms. Br J Pharmacol 173(15):2369–2389. https://doi.org/10.1111/bph.13514
14. Chen ML, Dong XH, Deng HY et al (2021) Targeting TRPV1-mediated autophagy attenuates nitrogen mustard-induced dermal toxicity. Signal Transduct Target Ther 6(1):29. https://doi.org/10.1038/s41392-020-00389-z
15. Hong Y, Ullah R, Wang JB et al (2023) Trends of obesity and overweight among children and adolescents in China. World J Pediatr 19(12):1115–1126. https://doi.org/10.1007/s12519-023-00709-7
16. Xu YX, Yu TH, Ma GJ et al (2021) Berberine modulates deacetylation of PPARγ to promote adipose tissue remodeling and thermogenesis via AMPK/SIRT1 pathway. Int J Biol Sci 17(12): 3173–3187. https://doi.org/10.7150/ijbs.62556

17. Johnson JM, Peterlin AD, Balderas E et al (2023) Mitochondrial phosphatidylethanolamine modulates UCP1 to promote brown adipose thermogenesis. Sci Adv 9(8):eade7864. https://doi.org/10.1126/sciadv.ade7864
18. Shamsi F, Xue RD, Huang TL et al (2020) FGF6 and FGF9 regulate UCP1 expression independent of brown adipogenesis. Nat Commun 11(1):1421. https://doi.org/10.1038/s41467-020-15055-9
19. Krishnan V, Baskaran P, Thyagarajan B (2019) Troglitazone activates TRPV1 and causes deacetylation of PPARγ in 3T3-L1 cells. Biochim Biophys Acta Mol Basis Dis 1865(2):445–453. https://doi.org/10.1016/j.bbadis.2018.11.004
20. Bertholet AM, Natale AM, Bisignano P et al (2022) Mitochondrial uncouplers induce proton leak by activating AAC and UCP1. Nature 606(7912):180–187. https://doi.org/10.1038/s41586-022-04747-5
21. Chen CC, Kuo CH, Leu YL et al (2021) Corylin reduces obesity and insulin resistance and promotes adipose tissue browning through SIRT-1 and β3-AR activation. Pharmacol Res 164:105291. https://doi.org/10.1016/j.phrs.2020.105291
22. Xue KL, Wu DM, Wang YS et al (2022) The mitochondrial calcium uniporter engages UCP1 to form a thermoporter that promotes thermogenesis. Cell Metab 34(9):1325–1341. https://doi.org/10.1016/j.cmet.2022.07.011
23. Wang Y, Yang SH, Zhong KY et al (2020) Network pharmacology-based strategy for the investigation of the anti-obesity effects of an ethanolic extract of *Zanthoxylum bungeanum* Maxim. Front Pharmacol 11:572387. https://doi.org/10.3389/fphar.2020.572387
24. Ren TY, Zhu YP, Xu FY et al (2023) The mechanisms of hydroxy-α-sanshool from *Zanthoxyum bungeanum maxim* activates AMPK-HIF1-PKM2 pathway to fix the obesity. J Funct Foods 107:105599. https://doi.org/10.1016/j.jff.2023.105599
25. Wang L, Fan WX, Zhang MM et al (2019) Antiobesity, regulation of lipid metabolism, and attenuation of liver oxidative stress effects of hydroxy-α-sanshool isolated from *Zanthoxylum bungeanum* on high-fat diet-induced hyperlipidemic rats. Oxid Med Cell Longev 2019:5852494. https://doi.org/10.1155/2019/5852494
26. Zhang Q, He CX, Wang LY et al (2023) Hydroxy-α-sanshool from the fruits of *Zanthoxylum bungeanum* Maxim. promotes browning of white fat by activating TRPV1 to induce PPAR-γ deacetylation. Phytomedicine 121:155113. https://doi.org/10.1016/j.phymed.2023.155113
27. Chruma JJ, Cullen DJ, Bowman L et al (2018) Polyunsaturated fatty acid amides from the *Zanthoxylum* genus – from culinary curiosities to probes for chemical biology. Nat Prod Rep 35(1): 54–74. https://doi.org/10.1039/c7np00044h
28. Luo JJ, Hou XY, Li SS et al (2022) Degradation and transformation mechanisms of numbing substances: hydroxyl-α-sanshool & hydroxyl-β-sanshool from *Zanthoxylum bungeanum* exposed to acid environment. Food Chem X 14:100342. https://doi.org/10.1016/j.fochx.2022.100342
29. Zhang MM (2019) Pharmacological Activity and Mechanism *Z. Bungeanum* Attenuated Scopolamine-Induced Cognition Impairments in Mice. MS Thesis, Chengdu University of Traditional Chinese Medicine, China (in Chinese). https://doi.org/10.26988/d.cnki.gcdzu.2019.000134
30. Francis TC, Yano H, Demarest TG et al (2019) High-frequency activation of nucleus accumbens D1-MSNs drives excitatory potentiation on D2-MSNs. Neuron 103(3):432–444. https://doi.org/10.1016/j.neuron.2019.05.031
31. Oh YM, Lee SW, Kim WK et al (2022) Age-related Huntington's disease progression modeled in directly reprogrammed patient-derived striatal neurons highlights impaired autophagy. Nat Neuro 25(11):1420–1433. https://doi.org/10.1038/s41593-022-01185-4
32. Tang FQ, Li LL, Chen D (2012) Mesoporous silica nanoparticles: synthesis, biocompatibility and drug delivery. Adv Mater 24(12):1504–1534. https://doi.org/10.1002/adma.201104763
33. Wang H, Chang XW, Ma Q et al (2022) Bioinspired drug-delivery system emulating the natural bone healing cascade for diabetic periodontal bone regeneration. Bioact Mater 21:324–339. https://doi.org/10.1016/j.bioactmat.2022.08.029
34. Kolonin MG, Saha PK, Chan L et al (2004) Reversal of obesity by targeted ablation of adipose tissue. Nat Med 10(6):625–632. https://doi.org/10.1038/nm1048
35. Won YW, Adhikary PP, Lim KS et al (2014) Oligopeptide complex for targeted non-viral gene delivery to adipocytes. Nat Mater 13(12):1157–1164. https://doi.org/10.1038/nmat4092
36. Meena KS, Dhanalekshmi KI, Jayamoorthy K (2016) Study of photodynamic activity of Au@SiO_2 core-shell nanoparticles in vitro. Mater Sci Eng C Mater Biol Appl 63(1):317–322. https://doi.org/10.1016/j.msec.2016.03.010
37. Mirenda M, Levi V, Bossi ML et al (2013) Temperature response of luminescent tris (bipyridine)ruthenium (II)-doped silica nanoparticles. J Colloid Interface Sci 392(1):96–101. https://doi.org/10.1016/j.jcis.2012.09.059
38. Mukhopadhyay S, Veroniaina H, Chimombe T et al (2019) Synthesis and compatibility evaluation of versatile mesoporous silica nanoparticles with red blood cells: an overview. RSC Adv 9(61): 35566–35578. https://doi.org/10.1039/c9ra06127d
39. Tang HX, Li CQ, Zhang Y et al (2020) Targeted manganese doped silica nano GSH-cleaner for treatment of liver cancer by destroying the intracellular redox homeostasis. Theranostics 10(21): 9865–9887. https://doi.org/10.7150/thno.46771
40. Li H, Zhu J, Xu YW et al (2022) Notoginsenoside R1-loaded mesoporous silica nanoparticles targeting the site of injury through inflammatory cells improves heart repair after myocardial infarction. Redox Biol 54:102384. https://doi.org/10.1016/j.redox.2022.102384
41. Vallet-Regí M (2022) Our contributions to applications of mesoporous silica nanoparticles. Acta Biomater 137:44–52. https://doi.org/10.1016/j.actbio.2021.10.011
42. Mi DD, Li JJ, Wang RJ et al (2023) Postsurgical wound the management and prevention of triple-negative breast cancer recurrence with a pryoptosis-inducing, photopolymerizable hydrogel. J Contr Release 356:205–218. https://doi.org/10.1016/j.jconrel.2023.02.042
43. Zhou J, Zhang J, Li JY et al (2021) Ginsenoside F2 suppresses adipogenesis in 3T3-L1 cells and obesity in mice via the AMPK pathway. J Agric Food Chem 69(32):9299–9312. https://doi.org/10.1021/acs.jafc.1c03420
44. Zhang Q, Li RL, Wang LY et al (2022) Hydroxy-α-sanshool isolated from *Zanthoxylum bungeanum* Maxim. has antidiabetic effects on high-fat-fed and streptozotocin-treated mice via increasing glycogen synthesis by regulation of PI3K/Akt/GSK-3β/GS signaling. Front Pharmacol 13:1089558. https://doi.org/10.3389/fphar.2022.1089558
45. Wang H, Yuan L, Hu N et al (2024) Effects of Jiaotai Pills on high-fat diet-induced hypothalamic inflammation in obese mice. Chin Trad Patent Med, early access (in Chinese). https://link.cnki.net/urlid/31.1368.R.20240206.1200.002
46. Zhu J, Chen XD, Zhao J (2024) The Fang's hypoglycemic formula

improves insulin resistance in type 2 diabetes mellitus by regulating mitochondrial autophagy. Integr Med Discov 8:e24016
47. Peng W, He CX, Li RL et al (2024) *Zanthoxylum bungeanum* amides ameliorates nonalcoholic fatty liver via regulating gut microbiota and activating AMPK/Nrf2 signaling. J Ethnopharmacol 318(Pt A):116848. https://doi.org/10.1016/j.jep.2023.116848
48. Lavie CJ, Milani RV, Ventura HO (2009) Obesity and cardiovascular disease: risk factor, paradox, and impact of weight loss. J Am Coll Cardiol 53(21):1925–1932. https://doi.org/10.1016/j.jacc.2008.12.068
49. Jiao WY, Mi S, Sang YX et al (2022) Integrated network pharmacology and cellular assay for the investigation of an anti-obesity effect of 6-shogaol. Food Chem 374:131755. https://doi.org/10.1016/j.foodchem.2021.131755
50. Parker KA, Ribet S, Kimmel BR et al (2022) Scanning transmission electron microscopy in a scanning electron microscope for the high-throughput imaging of biological assemblies. Biomacromolecules 23(8):3235–3242. https://doi.org/10.1021/acs.biomac.2c00323
51. Polletta L, Vernucci E, Carnevale I et al (2015) SIRT5 regulation of ammonia-induced autophagy and mitophagy. Autophagy 11(2): 253–270. https://doi.org/10.1080/15548627.2015.1009778
52. Peng W, Hu CL, Shu ZH et al (2015) Antitumor activity of tatariside F isolated from roots of *Fagopyrum tataricum* (L.) Gaertn against H22 hepatocellular carcinoma via up-regulation of p53. Phytomedicine 22(7–8):730–736. https://doi.org/10.1016/j.phymed.2015.05.003
53. Loomba R, Friedman SL, Shulman GI (2021) Mechanisms and disease consequences of nonalcoholic fatty liver disease. Cell 184(10):2537–2564. https://doi.org/10.1016/j.cell.2021.04.015
54. Canto C, Menzies KJ, Auwerx J (2015) NAD^+ metabolism and the control of energy homeostasis: a balancing act between mitochondria and the nucleus. Cell Metabolism 22(1):31–53. https://doi.org/10.1016/j.cmet.2015.05.023
55. Chen SZ, Liu XX, Peng C et al (2021) The phytochemical hyperforin triggers thermogenesis in adipose tissue via a Dlat-AMPK signaling axis to curb obesity. Cell Metabolism 33(3):565–580. https://doi.org/10.1016/j.cmet.2021.02.007
56. Qian D, Zhang Q, He CX et al (2024) *Hai-Honghua* medicinal liquor is a reliable remedy for fracture by promotion of osteogenic differentiation via activation of PI3K/Akt pathway. J Ethnopharmacol 330:118234. https://doi.org/10.1016/j.jep.2024.118234
57. Atanasov AG, Zotchev SB, Dirsch VM et al (2021) Natural products in drug discovery: advances and opportunities. Nat Rev Drug Disco 20(3):200–216. https://doi.org/10.1038/s41573-020-00114-z
58. Xie JQ, Huang JM, Wang C (2024) The potential of Chinese herbal medicines in treating anxiety disorders. Integr Med Discov 8:e24005. https://doi.org/10.53388/IMD202408005
59. Tian MZ, Ma ZC, Yang GZ (2024) Micro/nanosystems for controllable drug delivery to the brain. Innovation 5(1):100548. https://doi.org/10.1016/j.xinn.2023.100548
60. Gao Q, Feng J, Liu W et al (2022) Opportunities and challenges for co-delivery nanomedicines based on combination of phytochemicals with chemotherapeutic drugs in cancer treatment. Adv Drug Deliv Rev 188:114445. https://doi.org/10.1016/j.addr.2022.114445
61. Solomon D, Gupta N, Mulla NS et al (2017) Role of in vitro release methods in liposomal formulation development: challenges and regulatory perspective. AAPS J 19(6):1669–1681. https://doi.org/10.1208/s12248-017-0142-0
62. Tipnis NP, Shen J, Jackson D et al (2020) Flow-through cell-based in vitro release method for triamcinolone acetonide poly (lactic-co-glycolic) acid microspheres. Int J Pharm 579:119130. https://doi.org/10.1016/j.ijpharm.2020.119130